

# Direct numerical simulations of supersonic three-dimensional turbulent boundary layers

Salvador Rey Gomez®

Center for Turbulence Research, Stanford University, Stanford, CA 94305, USA Corresponding author: Salvador Rey Gomez, gomezsr@stanford.edu

(Received 27 March 2025; revised 4 August 2025; accepted 26 September 2025)

Supersonic turbulent channels subjected to sudden spanwise acceleration at initial friction Reynolds numbers of approximately 500 and different Mach numbers are studied through direct numerical simulations. The response to the spanwise acceleration creates a transient period where the flow exhibits three-dimensionality in the mean statistics. This enables a detailed study of the thermal transport and development of velocity transformations and Reynolds analogies for compressible turbulent flows in swept-like conditions. Extensions of velocity transformations to three-dimensional (3-D) flows demonstrate near-wall self-similarity of the velocity, providing evidence for Morkovin's hypothesis in nonequilibrium conditions. A similarity solution for the spanwise velocity, valid during the initial transient, is also presented. During the transient, both the thermal fluctuations and turbulent kinetic energy (TKE) decrease, consistent with previous observations in incompressible flows (Lozano-Durán et al. 2020 J. Fluid Mech. 883, A20, Moin et al. 1990 Phys. Fluids A: Fluid Dyn. 2, 1846–1853). For sufficiently strong spanwise acceleration,  $Q_3$  (+T', +v') and  $Q_1$  (-T', -v') events become more significant than sweep and ejections across the channel, creating changes in sign in the velocity-temperature covariances. The temporal evolution of the orientation and sizes of the TKE and temperature-carrying structures is quantified through structure identification and spectra. Finally, the generalized Reynolds analogy (Zhang et al. 2012 Phys. Rev. Lett. 109, 054502) is derived for a transient 3-D flow, allowing predictions of the mean temperature from the velocity.

**Key words:** turbulence modelling, turbulent boundary layers, compressible turbulence

#### 1. Introduction

Swept wings are commonly used in transonic and supersonic aircraft to delay or reduce high-speed drag and introduce mean three-dimensionality to the velocity statistics (Vos &

© The Author(s), 2025. Published by Cambridge University Press. This is an Open Access article, distributed under the terms of the Creative Commons Attribution licence (https://creativecommons.org/licenses/by/4.0/), which permits unrestricted re-use, distribution and reproduction, provided the original article is properly cited.

Farokhi 2015). Apart from swept wings, high speed applications also exhibit threedimensional (3-D) wall-bounded turbulent compressible flow when encountering surfacemounted obstacles (Subbareddy, Bartkowicz & Candler 2014), serpentine diffusers (Harrison et al. 2013) and rotating detonation engines (Bennewitz et al. 2018), to name but a few. Despite the engineering relevance of supersonic 3-D flows, the majority of detailed compressible turbulent flow studies focus on statistically planar flows where the mean velocity is in the streamwise and wall-normal directions. As a result, many of the models commonly used to predict velocity and thermal statistics are agnostic to effects stemming from spanwise accelerated flows. In this study, commonly used velocity-temperature relations and near-wall velocity transformations are extended to supersonic turbulent wall-bounded flows with swept-like conditions. These relationships are tested with direct numerical simulations (DNS) of fully developed statistically stationary compressible channels at moderate friction Reynolds number,  $Re_{\tau}$ , and subsonic and supersonic bulk Mach numbers, Ma, subjected to a sudden spanwise acceleration. During the transient response, the flow exhibits swept-like conditions as the flow adjusts to the new forcing direction.

Due to viscous heating, supersonic flows experience significant wall-normal mean temperature variation which in turn introduce wall-normal variation of the transport properties like the mean density and viscosity, as well as their fluctuations (Bradshaw 1977; Lele 1994; Anderson Jr. 2006). These property variations affect the velocity statistics in compressible flows. In compressible laminar boundary layer similarity solutions, the property variations are accounted for with similarity variables (Dorodnitsyn 1942; Lees 1956; Schlichting & Gersten 2016). In turbulent flows, Morkovin's (1962) hypothesis states that for sufficiently small turbulent Mach numbers or sufficiently small density fluctuations relative to the mean density, the compressible wall bounded turbulent flow can be mapped to an equivalent incompressible turbulent flow by accounting for property variations. These observations have inspired various velocity transformations in the literature that are able to apply the near-wall incompressible viscous scaling to compressible flows (Van Driest 1951; Zhang et al. 2012; Trettel & Larsson 2016; Griffin, Fu & Moin 2021; Hasan et al. 2023), some of which have been applied to flows with exotic property variations (Bai, Griffin & Fu 2022). In addition to velocity transformations, near-wall mean temperature fields have been shown to exhibit near-wall self-similarity when normalized with a friction temperature (Kader 1981; Kong, Choi & Lee 2000; Pirozzoli, Bernardini & Orlandi 2016). Further attempts to characterize and predict the temperature field began with the work of Reynolds (1874) who argued that the temperature is quadratically related to the velocity, developing the Reynolds analogy. This was shown to be true from compressible laminar flows (Busemann 1931; Crocco 1932). Further developments generalized the Reynolds analogy to non-unit Prandtl number and turbulent flows, even allowing for relations between the temperature and velocity fluctuations (Van Driest 1951; Morkovin 1962; Walz 1962; Gaviglio 1987; Huang, Coleman & Bradshaw 1995; Duan & Martin 2011; Zhang et al. 2014). These velocity transformations and Reynolds analogies focus primarily on statistically stationary two-dimensional (2-D) flows, and their extension to flows with temporal non-equilibrium or three-dimensionality has not received much attention. These studies can improve compressible wall-bounded turbulence modelling (Zhang et al. 2014; Griffin, Fu & Moin 2023), yet the lack of extensions to flows with 3-D effects can limit their predictive capability in realistic engineering applications (Lozano-Durán et al. 2020).

Statistically stationary 2-D flows have received much attention in turbulent studies as canonical flow configurations. Incompressible studies have developed and provided evidence of the mean velocity scaling and multiscale energetic motions in wall-bounded flows (von Kármán 1934; Millikan 1938; Coles 1956; Lee & Moser 2015) as well as various

tools to uncover the turbulent structure of the flow (Wallace, Eckelmann & Brodkey 1972; Lozano-Durán *et al.* 2012; Wallace 2016). Low *Ma* turbulent studies have been used to consider heat transfer and temperature transport as a passive scalar (Perry & Hoffmann 1976; Kader 1981; Nagano & Tagawa 1988; Kong *et al.* 2000; Pirozzoli *et al.* 2016). The majority of supersonic wall-bounded turbulent simulations have focused on supersonic boundary layers (Duan, Beekman & Martin 2010; Duan & Martin 2011; Pirozzoli & Bernardini 2011; Cogo *et al.* 2022) and channel flows (Coleman, Kim & Moser 1995; Huang *et al.* 1995; Modesti & Pirozzoli 2016; Yu, Xu & Pirozzoli 2019; Hasan *et al.* 2025), to name but a few. These studies have enabled detailed assessment and development of the velocity transformations and Reynolds analogies, while enabling studies of the turbulent structure and turbulent statistics.

Much of the studies of 3-D wall-bounded turbulent flows stem from incompressible studies. Initial experimental studies of swept-like conditions demonstrated a reduction in turbulent kinetic energy (TKE) and misalignment between the mean velocity and Reynolds shear stress directions (Bradshaw & Pontikos 1985). These studies were then corroborated with DNS of fully developed turbulent channels subjected to a sudden spanwise pressure gradient (Moin et al. 1990; Coleman, Kim & Le 1996; Lozano-Durán et al. 2020). These studies revealed that the reduction in the TKE, despite the net acceleration, occurs because of a decrease in the pressure-strain reducing the wall-normal velocity fluctuations that subsequently reduces the production of the streamwise Reynolds shear stress. This then reduces the production of the streamwise turbulent fluctuations faster than the spanwise turbulent fluctuations are generated. Structural studies have revealed that the reduction in the Reynolds shear stress can be attributed to a mismatch between the orientation of the near-wall small-scales and the larger structures farther from the wall. Additional cases of spanwise flows include drag-reduction studies where the walls are oscillated in the spanwise direction (Quadrio & Sibilla 2000; Choi, Xu & Sung 2002; Ge & Jin 2017; Marusic et al. 2021; Ricco, Skote & Leschziner 2021; Chandran et al. 2023; Rouhi et al. 2023), among others. The physical arguments that explain the reduction in the TKE in the spanwise accelerated channels are similar to those that explain the drag reduction in the spanwise oscillated channels. The spanwise oscillations have been used to study drag reduction in turbulent supersonic channel (Yao & Hussain 2019) and turbulent boundary layer (Ni et al. 2016) flows as well. However, compressible flows mimicking swept-like conditions through non-zero mean spanwise velocity are missing.

This paper uses DNS of fully developed compressible turbulent channels at an initial  $Re_{\tau} \approx 500$  and Ma = 0.3, 1.5 and 3.0 that are suddenly accelerated in the spanwise direction through a spanwise body force to study the temporal evolution of the velocity and temperature statistics. The paper is organized as follows. The configuration and numerical details are described in § 2. In § 3, the near-wall velocity transformations and temperature scaling are extended to transient 3-D flows. The mean velocity and temperature are then presented, along with a similarity solution for the spanwise flow, valid for initial times. The turbulent statistics and structural organization of the flow are discussed in § 4. The generalized Reynolds analogy (GRA) of Zhang *et al.* (2014) is extended to temporally varying, 3-D flows in § 5. Conclusions are presented in § 6.

## 2. Methodology

The compressible turbulent flow of a calorically perfect ideal gas within a channel is simulated with DNS using periodic streamwise and spanwise directions. The streamwise, wall-normal and spanwise coordinates are  $x \in [0, L_x]$ ,  $y \in [0, 2h]$ ,  $z \in [0, L_z]$ , respectively, where  $L_x$  and  $L_z$  are the channel dimensions and h the channel half-height.

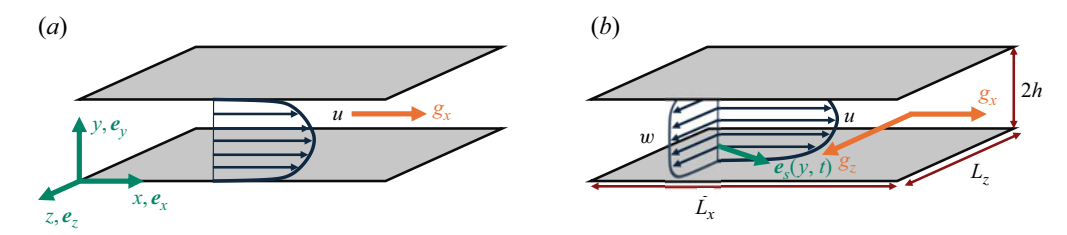


Figure 1. Schematic of the flow configuration and coordinates at t = 0 (a) and t > 0 (b).

The unit vectors  $e_x$ ,  $e_y$  and  $e_z$  are along the streamwise, wall-normal and spanwise directions, respectively. At time  $t \le 0$ , the flow is a fully developed canonical turbulent channel driven by a streamwise body force,  $g_x$ . For t > 0, a spanwise body force,  $g_z = \Pi g_x$  is applied which creates a transient period of 3-D mean flow. A schematic of these configurations is presented in figure 1. Driving the flow with body forces is analogous to the pressure gradients used in incompressible studies of 3-D transient flow (Moin et al. 1990; Lozano-Durán et al. 2020). Previous literature has also shown that driving a compressible channel with a body force gives only slight differences in the statistics compared with a pressure-driven one (Huang et al. 1995). For the flow to react solely to the imposed body forces, the commonly applied source term in the momentum equations that constrains the bulk mean velocity in compressible channel simulations (Coleman et al. 1995; Modesti & Pirozzoli 2016; Yu et al. 2019; Hasan et al. 2025) is omitted.

The flow evolves under the compressible Navier–Stokes equations,

$$\frac{\partial \rho}{\partial t} + \nabla \cdot (\rho \mathbf{u}) = 0, \tag{2.1}$$

$$\frac{\partial \rho \mathbf{u}}{\partial t} + \nabla \cdot (\rho \mathbf{u} \otimes \mathbf{u}) = -\nabla p + \nabla \cdot \tau + \rho \mathbf{g}, \tag{2.2}$$

$$c_{v}\left(\frac{\partial\rho T}{\partial t} + \nabla \cdot (\rho T \boldsymbol{u})\right) = -p\nabla \cdot \boldsymbol{u} - \nabla \cdot \boldsymbol{q} + \tau : \nabla \boldsymbol{u}, \tag{2.3}$$

along with the ideal gas law,  $p = \rho RT$ , and stress tensor,  $\tau = \mu(\nabla u^T + \nabla u - 2/3\nabla \cdot u\mathcal{I})$ , where  $\rho$  denotes the density, T the temperature, p the pressure,  $u = ue_x + ve_y + we_z$  the velocity with its respective components, R the universal gas constant,  $c_v$  the specific heat capacity at constant volume,  $\mu$  the dynamic viscosity,  $\mathbf{q} = q_x e_x + q_y e_y + q_z e_z$  the heat flux and  $\mathbf{g} = g_x e_x + g_z e_z$  the body force. For  $t \leq 0$ ,  $g_z = 0$  and t > 0,  $g_z = \Pi g_x$ . In (2.3), the cooling term that is commonly applied to the energy equation to enforce a constant bulk temperature (Coleman *et al.* 1995; Yu *et al.* 2019; Hasan *et al.* 2025) is omitted to also study the transient response in the temperature. The dynamic viscosity follows Sutherland's law

$$\frac{\mu(T)}{\mu_w} = \left(\frac{T}{T_w}\right)^{3/2} \frac{T_w + S}{T + S},\tag{2.4}$$

with S=110.4 K, and  $\mu_w$  is  $\mu$  evaluated at the wall. The heat flux follows Fourier's heating law,  $\mathbf{q}=-c_p\mu\nabla T/Pr$ , where  $c_p$  is the specific heat capacity at constant pressure and Pr=0.7 is the Prandtl number. At the bottom and top walls (y=0,2h), the flow satisfies the no-slip condition, the viscous boundary condition for pressure,  $\partial_y p=\partial_y \tau_{yy}$ , and the walls are isothermal with wall temperature  $T_w=300$  K.

Because the flow is temporally evolving as a response to the sudden spanwise acceleration, the statistics are averaged across the streamwise and spanwise directions. A quantity, f, can be decomposed via a Reynolds decomposition,  $f(x, y, z, t) = \overline{f}(y, t) + \overline{f}(y, t)$ 

f'(x, y, z, t), or a Favre decomposition,  $f(x, y, z, t) = \widetilde{f}(y, t) + f''(x, y, z, t)$  where the Reynolds average,  $\overline{f}$ , is

$$\overline{f}(y,t) = \frac{1}{L_x L_z} \int_0^{L_x} \int_0^{L_z} f(x, y, z, t) dz dx,$$
(2.5)

and the Favre average,  $\widetilde{f}$ , is

$$\overline{\rho}(y,t)\widetilde{f}(y,t) = \frac{1}{L_x L_z} \int_0^{L_x} \int_0^{L_z} \rho(x,y,z,t) f(x,y,z,t) dz dx.$$
 (2.6)

These averages are also averaged over the different ensembles and channel half-height, exploiting the symmetry or antisymmetry of f across y = h. Finally, the wall-normal average of a quantity g(y, t) is defined as

$$\langle g \rangle(t) = \frac{1}{h} \int_0^h g(y, t) dy. \tag{2.7}$$

This average is then used to define the bulk density,  $\rho_b = \langle \overline{\rho} \rangle$ , and bulk velocity,  $u_b = \langle \overline{\rho u} \rangle / \rho_b$ , where the former is constant in time from (2.1). Finally, a quantity with a subscript w or c is defined at the wall or centre such that  $f_w(t) = \overline{f}(0, t)$  and  $f_c(t) = \overline{f}(h, t)$ .

Due to the temporal transient, the mean flow direction,  $e_s$ , is a function of y and t. Here,  $e_s = e_1 e_x + e_3 e_z$  where  $e_1 = \overline{u}/\|\overline{u}\|$  and  $e_3 = \overline{w}/\|\overline{u}\|$ . At the wall,  $e_s$  is set to the mean shear direction such that  $e_1 = \overline{u}_y/\|\overline{u}_y\|$  and  $e_3 = \overline{w}_y/\|\overline{u}_y\|$  to avoid division by zero. Though different definitions can be prescribed for the instantaneous flow direction (Bradshaw & Pontikos 1985; Moin et al. 1990), this choice is used because of its interpretability and success in defining temporally local velocity transformations in § 3.1. To avoid confusion, the streamwise and spanwise directions here refer to  $e_x$  and  $e_z$ , respectively, while  $e_s$  is the mean flow direction. The wall shear stress is  $\tau_w = (\tau_{w,x}e_{w,1} + \tau_{w,z}e_{w,3})e_{s,w} = \tau_w e_{s,w}$ . The friction velocity is then  $u_\tau(t) = \sqrt{\tau_w/\rho_w}$  which introduces  $\ell_v(t) = \mu_w/\rho_w u_\tau$  as the viscous length scale. The speed of sound at the wall is  $a_w = \sqrt{\gamma R T_w}$ , where  $\gamma = 1.4$  is the ratio of specific heats. Henceforth, units of time with a + superscript will be normalized with the initial viscous time unit such that  $t^+ = t u_\tau(0)/\ell_v(0)$ . Finally, the use of the Einstein summation convention will be used where applicable with the indeces 1, 2 and 3 denoting streamwise, wall-normal and spanwise components.

## 2.1. Simulation set-up

The flow is studied with DNS using the HTR (hypersonics task-based research) solver code (Di Renzo *et al.* 2020). The flow is statistically stationary for  $t \le 0$  driven by  $g_x e_x$  to achieve a fixed friction Reynolds number,  $Re_\tau = \rho_w u_\tau h/\mu_w$ , and bulk Mach number,  $Ma = u_b/a_w$ . The semilocal Reynolds number,  $Re_\tau^* = \mu_c/\mu_w\sqrt{\rho_w/\rho_c}Re_\tau$  is not matched at  $t \le 0$ . The simulations use  $N_x = 768$ ,  $N_y = 256$  and  $N_z = 512$  grid points in x, y and z, respectively, where the discretization uses a sixth-order hybrid Euler scheme and the time stepping uses the strong-stability-preserving third-order Runge–Kutta scheme keeping the Courant–Friedrichs–Lewy number below 0.5. The points are uniform in x and z, while the wall-normal grid points are stretched as  $y = h \tanh(s_y \tilde{y})/\tanh(s_p)$  where  $\tilde{y} \in [-1, 1]$  are equispaced points. The stretching parameter  $s_y$  is chosen such that the first grid point away from the wall,  $\Delta y_{min}$ , has  $\Delta y_{min}/\ell_v(0) < 1$ .

From the initial stationary period, eight statistically independent snapshots separated in time by at least an eddy-turnover with a time separation of  $\Delta t \approx 550 \ell_{\nu}(0)/u_{\tau}(0)$  are

Cas	se $Re_{\tau}$	$Re_{\tau}^{*}$	Ма	П	$L_x$	$L_z$	$\Delta y_{min}/\ell_{\nu}(0)$	Style
1	505	497	0.3	10	$4\pi h$	$2\pi h$	0.34	
2	560	376	1.5	10	$4\pi h$	$2\pi h$	0.22	
3	550	179	3.0	10	$6\pi h$	$2\pi h$	0.25	
4	505	497	0.3	40	$4\pi h$	$2\pi h$	0.34	
5	560	376	1.5	40	$4\pi h$	$2\pi h$	0.22	
6	550	179	3.0	40	$6\pi h$	$2\pi h$	0.25	

Table 1. Streamwise and spanwise domain lengths,  $L_x$  and  $L_z$ , respectively; ratio of the driving body forces,  $\Pi = g_z/g_x$ ; smallest wall-normal grid spacing, and the initial  $Re_\tau$ ,  $Re_\tau^*$  and Ma for each simulation studied. In some figures, the cases are distinguished by the colours and line styles shown above.

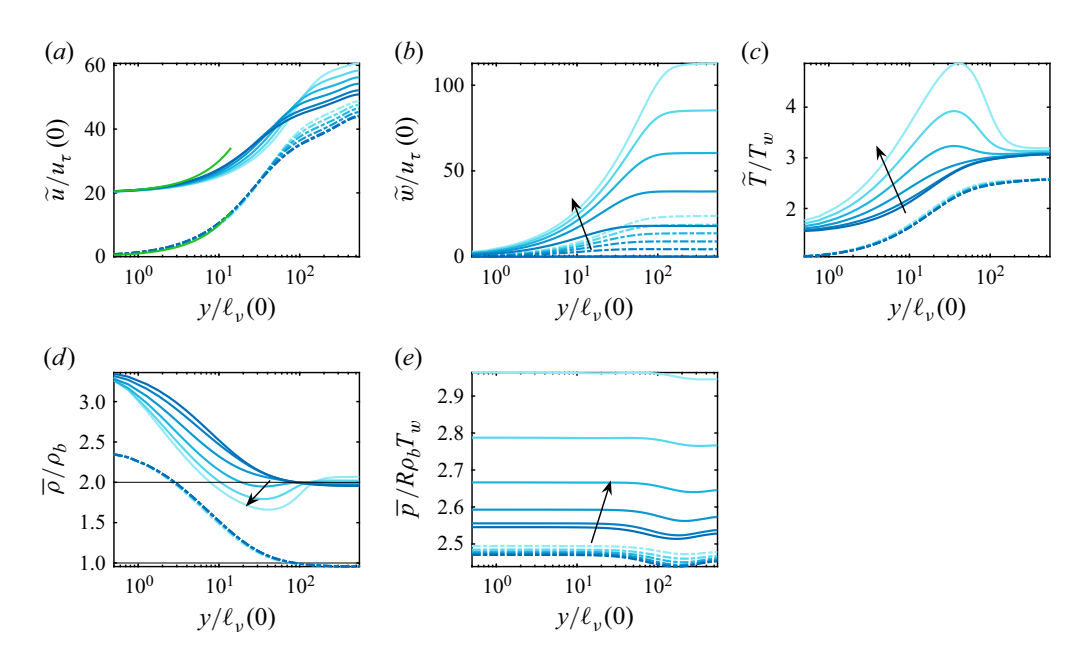


Figure 2. Temporal variation of  $\widetilde{u}$  (a),  $\widetilde{w}$  (b), normalized by the initial  $u_{\tau}$ ,  $\widetilde{T}$  normalized by  $T_w$  (c),  $\overline{\rho}$  normalized by  $\rho_b$  (d) and  $\overline{\rho}$  normalized by  $R\rho_bT_w$  (e) for Ma=3 and  $\Pi=10$  (dashed) and  $\Pi=40$  (solid). The plots of  $\Pi=40$  are offset vertically by 20, 0.5, 1 and .075 in (a), (c), (d) and (e), respectively, for visibility. The colours from dark to light and arrows indicate increasing time in increments of  $\Delta t^+=100$ . The green lines in (a) plot  $\overline{u}/u_{\tau}(0)=y/\ell_{\nu}(0)$ , the viscous sublayer for a canonical incompressible flow.

chosen to initialize the eight ensembles to average over. For t > 0, these initial conditions are integrated for a total time of  $550\ell_{\nu}(0)/u_{\tau}(0)$  and are driven by  $g_x e_x + \Pi g_x e_z$ . The  $L_x$ ,  $L_z$ ,  $\Pi$  and initial  $Re_{\tau}$  and Ma are listed in table 1. The grid resolution is similar to that used in Modesti & Pirozzoli (2016) at similar  $Re_{\tau}$ . The Ma = 3.0 cases use a longer streamwise domain because the increased  $\overline{\mu}$  make the local viscous length scales larger across the channel (Modesti & Pirozzoli 2016). Snapshots are saved in increments of  $\Delta t^+ = 10$  for postprocessing.

## 3. Scaling of the mean flow field

As a representative case, the mean flow fields of the  $\Pi=10$  and  $\Pi=40$ , Ma=3 channels are presented in figure 2 to highlight their temporal evolution and the wall-normal variation

in  $\overline{\rho}$  and  $\widetilde{T}$ . The other cases are presented in § 3.1 and are qualitatively similar to the Ma=3 cases. In figure 2(a,b),  $\widetilde{u}$  and  $\widetilde{w}$  are plotted, normalized by the initial  $u_{\tau}$ . Due to the sudden application of  $g_z$ ,  $\widetilde{w}$  increases monotonically with time throughout the channel for both  $\Pi$ . For  $\widetilde{u}$ ,  $g_z$  primarily affects the outer region with a more pronounced effect for  $\Pi=40$ . Similarly, the effect of  $g_z$  on  $\widetilde{T}$  is most appreciable for  $\Pi=40$  in figure 2(c), attaining a local near-wall temperature peak commonly observed in turbulent boundary layers (Duan et al. 2010; Cogo et al. 2022). Due to the increase in viscous heating opposing the spanwise acceleration,  $\widetilde{T}$  increases with t. The density decreases in the near-wall region, and increases in the outer region to maintain a constant  $\rho_b$ , as shown in figure 2(d). The net increase in  $\widetilde{T}$  increases  $\overline{p}$ , despite the constant  $\rho_b$ . In the following sections, the temporal evolution and property variations are accounted for in  $\widetilde{u}$  and  $\widetilde{T}$  using viscous scaling, velocity transformations and self-similar solutions.

## 3.1. Extension of velocity-transformations to 3-D non-equilibrium flows

Morkovin's (1962) hypothesis has inspired various velocity transformations for statistically stationary 2-D flows, like channels and boundary layers, using mean property variations to collapse the compressible mean velocity onto an equivalent incompressible mean velocity in the near-wall region (Van Driest 1951; Zhang *et al.* 2012; Trettel & Larsson 2016; Griffin *et al.* 2021; Hasan *et al.* 2023). However, extensions to statistically 3-D or temporally varying compressible flows have not yet been applied in the literature. Previous studies in transient 3-D non-equilibrium incompressible flows have shown that the initial  $u_{\tau}$  and  $\ell_{\nu}$  do not appropriately collapse the near-wall  $\overline{u}$  (Lozano-Durán *et al.* 2020), while rescaling the 3-D velocity magnitude,  $\|\overline{u}\|$ , with the local  $u_{\tau}(t)$  and  $\ell_{\nu}(t)$  can collapse the near-wall statistics to the canonical counterpart (Moin *et al.* 1990). This suggests that an appropriate compressible velocity transformation for the near-wall region must be local in time and account for the variation in the transport properties.

First, the mean stress balance is projected along the mean flow direction as

$$\boldsymbol{e}_{s} \cdot \int_{0}^{y} \frac{\partial \overline{\rho} \widetilde{\boldsymbol{u}}}{\partial t} dy + \boldsymbol{e}_{s} \cdot (\overline{\rho} \widetilde{\boldsymbol{v}} \widetilde{\boldsymbol{u}} + \overline{\rho} \widetilde{\boldsymbol{v}} \widetilde{\boldsymbol{u}}'') = \boldsymbol{e}_{s} \cdot (\overline{\tau} \boldsymbol{e}_{y} - \boldsymbol{\tau}_{w}) + \boldsymbol{e}_{s} \cdot \int_{0}^{y} \overline{\rho} \boldsymbol{g} dy. \tag{3.1}$$

Now this stress balance is considered in a region where  $y \ll h$ . In this region,  $\rho \tilde{v} \tilde{u} + \rho \tilde{v}'' \tilde{u}''$  is negligible because of the no slip condition. The no slip condition also causes  $\int_0^y \rho g \, dy \sim O(y)$  and  $\int_0^y \partial \rho \tilde{u}/\partial t \, dy \lesssim O(y)$ . Furthermore,  $\overline{\tau} e_y \approx \overline{\mu} \partial_y \tilde{u}$  such that the dominant stress balance is  $\overline{\mu} \partial_y \|\tilde{u}\| = e_s \cdot \tau_w$ . This implies that the near-wall  $\|\tilde{u}\|$  should be agnostic to the spanwise acceleration and determined only by its viscous scales,  $u_\tau(t)$  and  $\ell_v(t)$ , and the near-wall mean property variations. Since the time derivatives are negligible here, the transport properties and viscous scales can be assumed to be quasisteady. In figure 3(a,b)  $\|\tilde{u}\|$  is plotted using the incompressible viscous scaling by normalizing with  $u_\tau(t)$  and  $\ell_v(t)$ . These wall-evaluated scales are not capable of ensuring near-wall self-similarity as even near  $y/\ell_v(t) = 10$ , the Ma = 3.0 profiles begin to depart from the incompressible law-of-the-wall. While outer-layer self-similarity is not ensured with these viscous scales, even for an incompressible flow (Lozano-Durán *et al.* 2020), these wall-scaled flows exhibit a clear Ma dependence in the wakes seen most prominently in the  $\Pi = 10$  cases in figure 3(a).

Based on the mean-stress balance and observations of near-wall self-similarity in the incompressible spanwise accelerated flow (Moin *et al.* 1990), a velocity transformation is pursued using the Trettel & Larsson (2016) (TL) velocity transformation. In Gomez (2025), the Griffin *et al.* (2021) (GFM) velocity transformation was presented. By construction, the GFM and TL transformations are equivalent near the wall where the

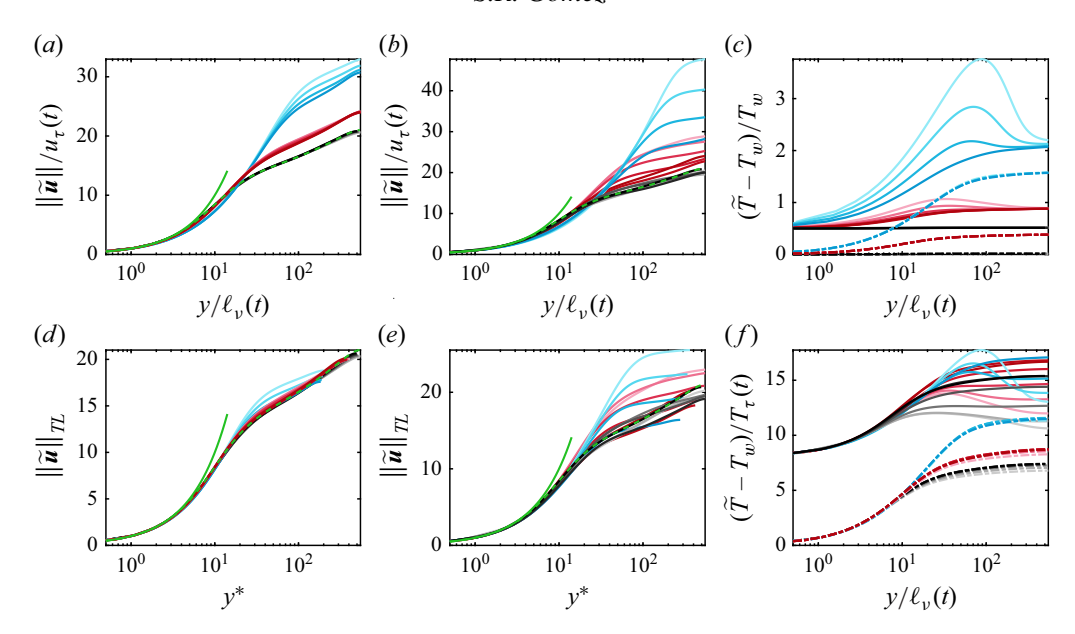


Figure 3. Quasisteady friction scaling of  $\|\tilde{\boldsymbol{u}}\|$  for  $\Pi=10$  (a) and  $\Pi=40$  (b). Here  $\widetilde{T}$  normalized by  $T_w$  with y normalized by  $\ell_v(t)$  (c). The TL transformation of  $\|\tilde{\boldsymbol{u}}\|$  for  $\Pi=10$  (d) and  $\Pi=40$  (e) and friction scaling of  $\widetilde{T}$  by normalizing with  $T_{\tau}(t)$  (f). The colours and line styles follow from table 1. The colours from dark to light are offset by time increments of  $\Delta t^+=100$ . In (a), (b), (d) and (e), the green line plots the viscous sublayer of an incompressible flow as  $u^+=y^+$  and the green dashed line plots the mean velocity of an  $Re_{\tau}=550$  turbulent channel (Lee & Moser 2015).

self-similarity is expected to hold. With the TL transformation, the compressible mean stress balance is assumed to map to an equivalent incompressible balance as  $\mu_w d\|\widetilde{\boldsymbol{u}}\|_{TL}/dy^* = \overline{\mu}\ell_v/u_\tau \ \partial\|\widetilde{\boldsymbol{u}}\|\partial y = 1$  where  $y^* = \sqrt{\overline{\rho}/\rho_w}\mu_w/\overline{\mu}y/\ell_v(t)$  is the semilocal coordinate and  $\|\widetilde{\boldsymbol{u}}\|_{TL}$  the transformed velocity. Following arguments from Trettel & Larsson (2016), the velocity transformation is then

$$\|\widetilde{\boldsymbol{u}}\|_{TL} = \frac{1}{u_{\tau}} \int_{0}^{y} \sqrt{\frac{\overline{\rho}}{\rho_{w}}} \left( 1 + \frac{1}{2} \frac{1}{\overline{\rho}} \frac{\partial \overline{\rho}}{\partial y} y' - \frac{1}{\overline{\mu}} \frac{\partial \overline{\mu}}{\partial y} y' \right) \frac{\partial \|\widetilde{\boldsymbol{u}}\|}{\partial y} dy', \tag{3.2}$$

where all the properties and wall quantities are evaluated locally in time. This transformation omits any viscous-scaling in t since temporal gradients are not present in the mean stress balance close to the wall. The Zhang et al. (2012) and Van Driest (1951) velocity transformations do not create an analogous transformation between the compressible and incompressible mean stress balance, thus they are not applicable here. In figure 3(d,e), the TL transformation is applied, illustrating an improved near-wall collapse to the wall scaling from figure 3(a,b). For the  $\Pi=10$  cases, the TL transformation mitigates the Ma dependence in the wakes collapsing them closer to the incompressible canonical flow in green. While the collapse in the near-wall region improves for the  $\Pi = 40$  case up to  $y^* = 10$  by reducing the wake and bringing the buffer layer closer to the wall for the supersonic cases, the rapid evolution in the wake limits the transformation from extending farther from the wall. As evidenced in (3.1), away from the wall the acceleration terms are dominant and not governed by viscous scales. Thus, velocity transformations relying on viscous scales cannot collapse the wake in strongly accelerated flows, even for incompressible flows. However, wake-deficit scaling with outer units was shown to collapse the wake in Gomez (2025).

Following the success of the quasisteady scaling in the velocities and the use of the friction temperature in the literature (Kader 1981; Kong *et al.* 2000; Pirozzoli *et al.* 2016), a quasisteady friction temperature,  $T_{\tau}$ , is presented. The assumption here is that the near-wall temperature is governed by the total wall-shear stress such that  $T_{\tau}(t) = q_w(t)/(c_p\rho_w(t)u_{\tau}(t))$ . This temperature scale is presented in figure 3(f) for  $\widetilde{T}$  where the wall-normal coordinate is normalized by  $\ell_{\nu}(t)$ . The near-wall collapse in  $\widetilde{T}$  suggests that the near-wall temperature is also influenced by its friction scales and mean flow direction. The Ma = 1.5 and Ma = 0.3 cases also exhibit a near-wall  $\widetilde{T}$  peak for  $\Pi = 40$ . The emergence of this peak is casused by elevated viscous heating due to the significant increase in turbulent intensities attributed with the  $\Pi = 40$  case after the initial decrease discussed in § 4.1.

# 3.2. A self-similar velocity transformation for the spanwise velocity

The x- and z-averaged spanwise momentum equation is

$$\frac{\partial}{\partial t}(\overline{\rho}\widetilde{w}) + \frac{\partial}{\partial y}(\overline{\rho}\widetilde{w''v''}) + \frac{\partial}{\partial y}(\overline{\rho}\widetilde{w}\widetilde{v}) - \overline{\rho}g_z = \frac{\partial\overline{\tau}_{yz}}{\partial y} = \frac{\partial}{\partial y}\left[\overline{\mu}\frac{\partial\overline{w}}{\partial y} + \overline{\mu'\frac{\partial w'}{\partial y}} + \overline{\mu'\frac{\partial v'}{\partial z}}\right].$$
(3.3)

Due to mass conservation and an unsteady  $\overline{\rho}$ ,  $\widetilde{v}$  is non-zero for t>0. However, the magnitude of  $\widetilde{v}$  remains negligible compared with  $\widetilde{w}$  and  $\widetilde{u}$  and its contribution is omitted for the rest of this section. For  $t \leq 0$ , the spanwise Reynolds shear stress,  $\overline{\rho}\widetilde{w''v''}$ , and spanwise turbulent viscous stresses,  $\overline{\mu'\partial_y w'} + \overline{\mu'\partial_z v'}$ , are initially zero due to the lack of net transport in the spanwise homogeneous direction and spanwise homogeneity. As time advances, the development of  $\widetilde{w}$  will lead to the generation of  $\overline{\rho}\widetilde{v''w''}$  (Moin *et al.* 1990; Lozano-Durán *et al.* 2020) and turbulent viscous stresses via the net transport of  $\mu'$  in  $e_z$  through  $\overline{\mu'\partial_y w'}$ , though the latter are negligible (Bradshaw 1977).

The time evolution of these terms is shown in figure 4(a-c) for  $\Pi=40$  and the three Ma. The acceleration term,  $\partial_t(\overline{\rho}\widetilde{w})$ , is estimated from the saved snapshots using finite differencing. The acceleration term primarily balances  $\overline{\rho}g_z$  in the outer region of the flow, while for short times, the viscous stress balances  $\overline{\rho}g_z$  near the wall. As time advances,  $\overline{\rho}v''w''$  intensifies, balancing the viscous stresses. This can be seen more clearly in figure 4(d-f) where the magnitudes of each of the terms is integrated in y to measure their effect across the channel. These plots show a period where the spanwise Reynolds stresses are negligible. An estimate for  $\overline{\tau}_{yz}$  via  $\overline{\mu}\partial_y\overline{w}$  is included, demonstrating that the turbulent viscous stresses are indeed negligible (Bradshaw 1977). Hence, for a short time interval, the effect of the Reynolds stresses and turbulent viscous stresses on the spanwise momentum equation may be neglected. For the supersonic cases, this interval extends much longer than the Ma=0.3 case due to the increase in near-wall viscosity that dampens the production of the spanwise Reynolds shear stress. The time interval,  $t_I$ , is defined as the time where  $\int_0^{2h} \left|\partial_y \overline{\tau}_{yz}\right| dy = \int_0^{2h} \left|\partial_y (\overline{\rho}w''v'')\right| dy$ , that is the time where the viscous stress is no longer dominant over the Reynolds stress.

To model the initial development of the spanwise mean flow for  $t \ll t_I$ , several assumptions are made. Following the observations from figure 4, it is assumed that the turbulent viscous stresses can be neglected such that  $\overline{\tau}_{yz} \approx \overline{\mu} \partial_y \widetilde{w}$  and that  $\overline{\rho} \widetilde{v''w''}$  is negligible compared with  $\overline{\tau}_{yz}$ . The third assumption is that the mean properties are quasisteady. This means that  $\overline{\rho}$  and  $\overline{\mu}$  are treated as constant in time with their values updated locally at each time and their temporal gradients are negligible. Finally, it

## S.R. Gomez

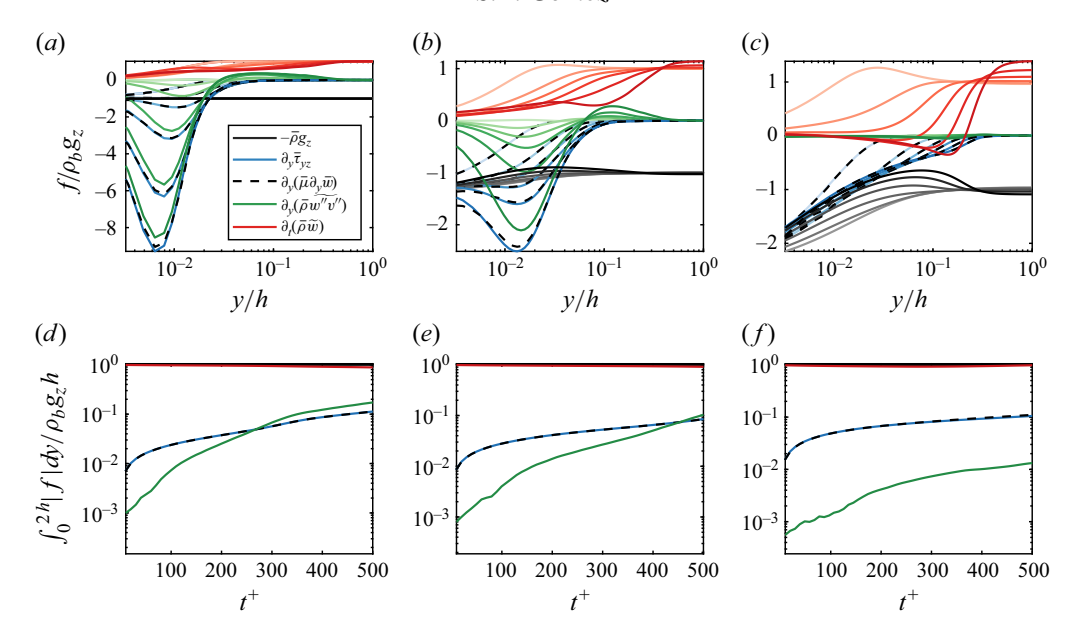


Figure 4. Spanwise mean momentum balance for  $\Pi = 40$  and Ma = 0.3 (a,d), 1.5 (b,e), 3.0 (e,f). In (a)–(c), the colours from dark to light denote different time instances, in increments of  $\Delta t^+ = 100$ . The quantity, f, is labelled in the legend of (a).

is assumed that density fluctuations play a minor role such that  $\overline{w} \approx \widetilde{w}$ . With these approximations, (3.3) can be simplified as

$$\frac{\partial \widetilde{w}}{\partial t} - g_z = \frac{1}{\overline{\rho}} \frac{\partial}{\partial y} \left[ \overline{\mu} \frac{\partial \widetilde{w}}{\partial y} \right]. \tag{3.4}$$

These assumptions essentially assume that a laminar prediction for  $\widetilde{w}$  holds. This has been shown to hold only for short times in incompressible simulations similar to the cases studied here (Moin *et al.* 1990; Lozano-Durán *et al.* 2020) and for spanwise oscillating walls in drag reduction (Quadrio & Sibilla 2000; Choi *et al.* 2002). The extent of the laminar prediction is expected to hold for a much longer time for the supersonic cases because of the larger  $t_I$ .

In Gomez (2025), (3.4) was solved using separation of variables and a series solution with the eigenmodes of  $1/\overline{\rho}\partial_y[\overline{\mu}\partial_y]$ . The series solution is an exact solution to (3.4) under the assumptions described above. Here, a similarity solution is presented which provides a velocity transformation for  $\widetilde{w}$ . First, it is assumed that

$$\widetilde{w} = g_z t f(\eta) \tag{3.5}$$

where

$$\eta(y,t) = \sqrt{\frac{\overline{\rho}(y)\overline{\mu}(y)}{t}} \int_0^y \frac{\mathrm{d}\xi}{\overline{\mu}(\xi)}$$
(3.6)

is the similarity variable and the explicit time dependence of  $\overline{\mu}$  and  $\overline{\rho}$  is neglected. For an incompressible flow with constant transport properties,  $\eta_{inc}(y, t) = y/\sqrt{\overline{\nu}t}$ , where  $\nu = \mu/\rho$  is the kinematic viscosity, is the same similarity variable as that used in Stoke's first problem (Schlichting & Gersten 2016). The similarity variable  $\eta$  is different to the one introduced by the Lees–Dorodnitsyn transformation (Dorodnitsyn 1942; Lees 1956; Anderson Jr. 2006; Schlichting & Gersten 2016), even when converting x to  $u_e t$ , because

the quantity in the square-root is wall-normally varying and the integrand is  $\overline{\mu}^{-1}$  rather than  $\overline{\rho}$ . It can then be shown that using (3.5), (3.4) becomes

$$f - \frac{\eta}{2} \frac{\mathrm{d}f}{\mathrm{d}\eta} - 1 = \frac{\mathrm{d}^2 f}{\mathrm{d}\eta^2}.$$
 (3.7)

Note that (3.7) is the same for both incompressible and compressible flow. The difference in the solutions is the similarity variable,  $\eta$ . Reducing (3.5) to the same incompressible similarity equation via  $\eta$  demonstrates the applicability of Morkovin's (1962) hypothesis where the same incompressible mechanisms govern the compressible spanwise response, provided that the mean property variations are accounted for.

For (3.5) to be a valid solution, it must satisfy the no-slip boundary conditions at y = 0, 2h and the initial condition  $\widetilde{w} = 0$  at t = 0. Since (3.7) is a second-order differential equation, it can only satisfy two boundary conditions. To reconcile the boundary condition at y = 2h, the solution proposed in (3.5) will only be valid for  $y \in [0, h]$  and  $\widetilde{w}$  will be assumed to be an even function in y about y = h so that its wall-normal derivative is continuous. The boundary condition at y=0 and the initial condition at t=0 on  $\widetilde{w}$ translate to the boundary conditions that f = 0 at  $\eta = 0$  and f = 1 at  $\eta \to \infty$ , respectively. The latter condition ensures that f is bounded as  $t \to 0$ . Due to the additional assumption of symmetry about y = h, there is an additional constraint that  $df/d\eta = 0$  at  $\eta(h, t)$ . This presents an additional boundary condition that cannot be reconciled analytically. However, it will be assumed that  $\eta(h, t) \gg 1$  so that this symmetry constraint becomes equivalent to  $df/d\eta = 0$  as  $\eta \to \infty$ . This is equivalent to assuming that the viscous length scales in the laminar solution are much smaller than h. An order of magnitude estimate for  $\eta(h, t)$  can be found using viscous wall units and approximating  $\eta$  with the incompressible counterpart as  $\eta(h, t) \sim h/\sqrt{\overline{v}t} = Re_{\tau}/\sqrt{t^+}$ . The smallest  $\eta(h, t)$  can be is at  $t^+ \approx 550$  during the duration of the simulation, which for the cases studied here is  $\eta \approx Re_{\tau}/\sqrt{550} \approx 23$ . It will be shown that for this estimate,  $df/d\eta = 0$  can be satisfied to numerical round off error.

The solution to (3.7) that satisfies the boundary conditions at  $\eta = 0$  and  $\eta \to \infty$  is

$$f = 1 - \left(\frac{\eta^2}{2} + 1\right) \operatorname{erfc}\left(\frac{\eta}{2}\right) + \frac{\eta}{\sqrt{\pi}} e^{-\frac{\eta^2}{4}},$$
 (3.8)

where erfc is the complimentary error function (Boas 2006). The solution's derivative,  $\mathrm{d}f/\mathrm{d}\eta = 2/\sqrt{\pi} \exp(-\eta^2/4) - \eta \mathrm{erfc}(\eta/2)$ , using the incompressible estimate of  $\eta \approx 23$  evaluates to  $O(10^{-60})$ . The smallest value for all six compressible cases is  $\eta(h,t) \approx 10$  at the end of the simulation, which evaluates  $\mathrm{d}fd/\eta \approx 10^{-13}$ . Though not exactly zero, it is a sufficient approximation for symmetry about y = h. The value of  $\eta(h,t)$  is much larger during the interval  $t \in [0,t_I]$  where the laminar assumptions are expected to hold which only improves the approximation regarding symmetry about y = h.

The instantaneous  $\widetilde{w}$  are plotted in figure 5(a,b) for all six cases, normalized by  $g_z t$ , against  $\eta(y,t)$ . The similarity solution, f, is also included where  $\eta$  is evaluated using (3.6) for the compressible solution and  $\eta_{inc}$  to illustrate an incompressible approximation. For short time intervals,  $f(\eta)$  and  $\widetilde{w}/g_z t$  agree because of the absence of spanwise turbulent stresses for all six cases. As time advances, the laminar approximation breaks creating departures from the compressible-laminar similarity solution. This departure is most severe in the Ma=0.3 cases where  $t_I$ , the time it takes  $\overline{\rho} v''w''$  to dominate over  $\overline{\tau}_{yz}$ , is smallest. For the Ma=3 cases,  $\widetilde{w}/g_z t$  and  $f(\eta)$  agree during the full simulation time as  $\overline{\rho} v''w''$  remains negligible compared with  $\overline{\tau}_{yz}$ . Although figure 2(a) demonstrates significant temporal variation in  $\overline{\rho}$  for case 6, the agreement between the data and the

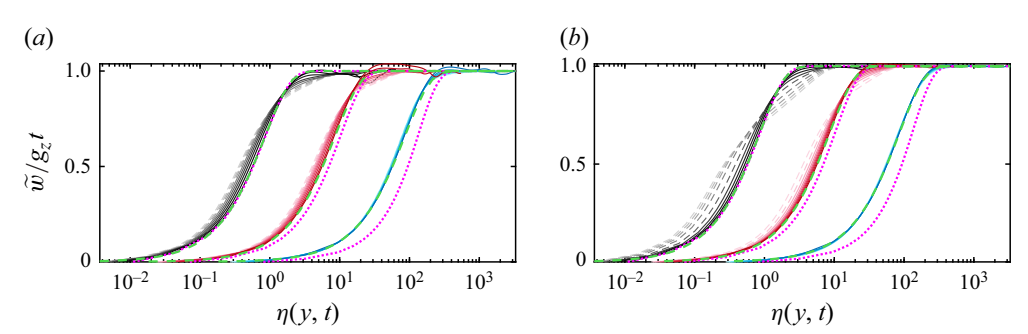


Figure 5. Similarity scaling of the spanwise flow for (a)  $\Pi = 10$  and (b)  $\Pi = 40$ . The solid and dashed lines colour coded with table 1 are DNS data, with the dashed lines plotted for  $t > t_I$ , and colours from dark to light indicate increasing time, plotted from  $t^+ = 60$  in increments of  $\Delta t^+ = 60$ . The green dashed line is the compressible similarity solution,  $f(\eta(y, t))$ . The magenta dotted line is the incompressible similarity solution,  $f(\eta_{inc}(y, t))$ , against  $\eta(y, t)$  at  $t^+ = 60$ . The Ma = 1.5 and Ma = 3.0 cases are offset horizontally for visibility.

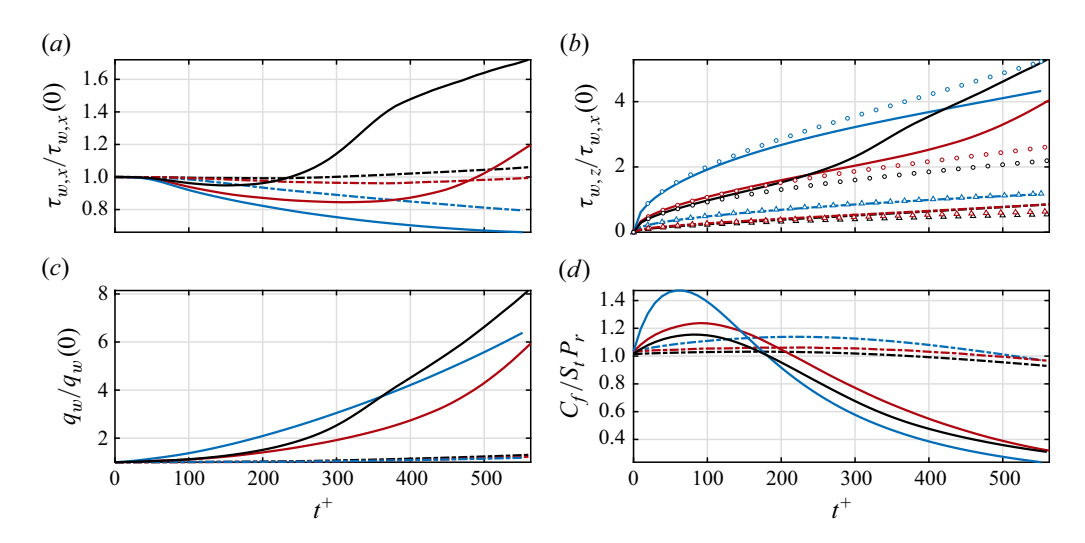


Figure 6. Temporal variation of (a)  $\tau_{w,x}$ , (b)  $\tau_{w,z}$ , (c)  $q_w$  and (d)  $C_f/(S_t Pr)$ . In (b), the symbols denote the laminar prediction,  $2g_z\sqrt{\rho_w\mu_wt/\pi}$ , with the circles and triangles denoting  $\Pi=40$  and  $\Pi=10$ , respectively. The colours and line styles are defined in table 1.

similarity solution demonstrates that the quasisteady approximation is valid and any discrepancies in the smaller Ma flows are indeed from the turbulent stresses. Finally, the incompressible solution,  $f(\eta_{inc})$ , agrees well with the Ma=0.3 cases, but exhibits significant departures from  $f(\eta)$  and  $\widetilde{w}/g_z t$  in the near-wall region as the Ma increases. Properly accounting for the mean property variations in  $\eta$  allows the similarity solution, f, to accurately predict  $\widetilde{w}$  for small times.

## 3.3. Mean shear and heat transfer

The evolution of  $\tau_{w,x}$  is shown in figure 6(a) for all six cases. The temporal evolution of  $\tau_{w,x}$  depends both on Ma and  $\Pi$  and is a direct result of the evolution of  $u_b$ , which is not here constrained as the streamwise flow is driven with a constant  $g_x$ . In incompressible studies of sudden spanwise acceleration (Lozano-Durán *et al.* 2020) and in the drag

reduction observed in spanwise oscillations with constant dp/dx (Ge & Jin 2017; Ricco et al. 2021),  $\tau_{w,x}$  is also affected by the spanwise acceleration.

Owing to the success of the laminar prediction of  $\widetilde{w}$  for initial times, a laminar prediction of  $\tau_{w,z}$  is also included via  $\tau_{w,z} = \mu_w g_z \partial_y f(\eta)|_{y=0} = 2g_z \sqrt{\rho_w \mu_w t/\pi}$  in figure 3(b). This prediction agrees well for  $\Pi=10$  and for  $\Pi=40$  begins to deviate substantially for  $t < t_I$  despite the success of the similarity solutions. The departure is present even for Ma=3, indicating discrepancies in the near-wall prediction of  $\widetilde{w}$  from the similarity solution because of the production of turbulent stresses. Due to the net acceleration in the flow,  $\tau_{w,z}$  increases monotonically during the transient. The increase in kinetic energy then results in additional viscous heating (Lele 1994), raising both  $\overline{T}$  and  $q_w$ , as shown in figure 6(c). The temporal evolution of  $\tau_{w,z}$  and  $q_w$  show more similarity for matched value of  $\Pi$  rather than Ma.

A common predictive tool in turbulent boundary layers is the Reynolds analogy factor, relating the friction coefficient,  $C_f$  and the Stanton number,  $S_t$  (Bradshaw 1977). While Fanning flow uses a friction coefficient based on the bulk velocity, here  $C_f$  is related to the centreline quantities as an analogy for the free stream conditions. Here,  $C_f = 2\|\mathbf{\tau}_w\|/(\rho_c\|\widetilde{\boldsymbol{u}}_c\|^2)$  and  $S_t = q_w/(\rho_c c_p\|\widetilde{\boldsymbol{u}}_c\|(T_c - T_w))$ . Other definitions for these quantities have been used in the literature, primarily in the context of boundary layers. The ratio,  $C_f/S_t Pr$ , begins at 1 and promptly evolves as  $g_z$  is applied in figure 3(d). The Reynolds analogy factor,  $f_{RA} = 2S_t/C_f$ , (Bradshaw 1977) is observed to be approximately 2Pr for the canonical channels simulated herein at t=0 and during the simulation time of the  $\Pi=10$  cases whereas  $f_{RA}$  varies significantly for  $\Pi=40$ . The choice of  $C_f$  and  $S_t$  is non-unique. It is possible that different choices could lead to a constant ratio throughout the simulation time, though this is outside of the scope of this work.

### 4. Turbulent fluctuations

Apart from changing the mean quantities, the spanwise acceleration also affects the turbulent structure throughout the channel. As a motivating picture, the instantaneous velocity and temperature fluctuation fields of Ma = 1.5 and  $\Pi = 40$  at two different wall-normal heights are shown in figure 7(a-h) for the canonical state at t = 0 and  $t^+ = 415$ , where the spanwise flow has become significant. Qualitatively, the near-wall plane in figure 7(b,d) demonstrate structures more uniformly aligned with the direction of the flow than the structures in the log-layer plane in figure 7(f,h). In the near-wall planes, the u' and T' fields demonstrate a strong degree of correlation for both  $t^+ = 0$  and  $t^+ = 415$ . The correlated u' and T' fields are also present at  $t^+ = 0$  for the log-layer plane. Due to the acceleration from the spanwise flow, these fields are anticorrelated at  $t^+ = 415$ . These qualitative observations from the instantaneous flows motivate the quantitative measures in the rest of this section.

## 4.1. *Drop in TKE and thermal fluctuations*

Spanwise acceleration has been shown to reduce the TKE via flow control strategies with active walls (Quadrio & Sibilla 2000; Choi *et al.* 2002; Ge & Jin 2017; Marusic *et al.* 2021; Ricco *et al.* 2021; Chandran *et al.* 2023; Rouhi *et al.* 2023) or the initial development of a spanwise flow (Bradshaw & Pontikos 1985; Moin *et al.* 1990; Coleman *et al.* 1995; Lozano-Durán *et al.* 2020). From the sudden spanwise acceleration, incompressible studies (Moin *et al.* 1990; Lozano-Durán *et al.* 2020) have concluded that due to the spanwise flow, the pressure-strain term,  $p'\partial_z v'$ , drops, leading to a reduction in v'v'. This

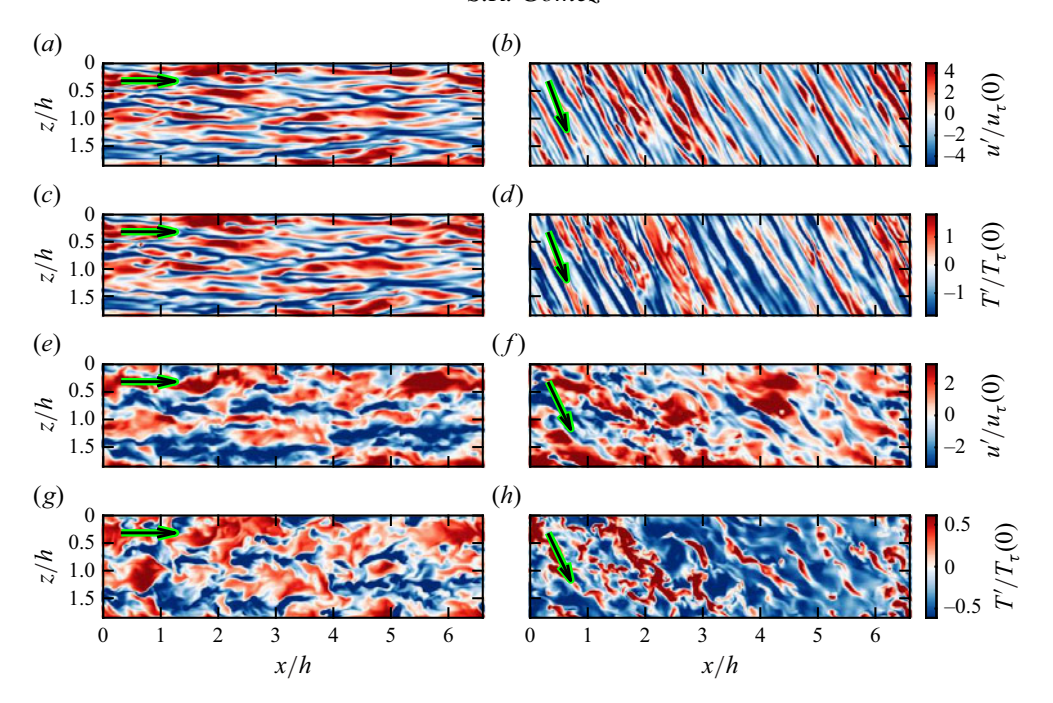


Figure 7. Instantaneous flow fields of (a,b,e,f)  $u'/u_{\tau}(0)$  and (c,d,g,h)  $T'/T_{\tau}(0)$  for Ma=1.5 and  $\Pi=40$ . The planes in (a)-(d) are at  $y/\ell_{\nu}(0)=15$ , (e)-(h) are at  $y/\ell_{\nu}(0)=100$ , (a), (c), (e) and (g) are at  $t^+=0$  and (b), (d), (f) and (h) are at  $t^+=415$ . The black arrow denotes the instantaneous direction of  $\widetilde{\boldsymbol{u}}$  at the wall-normal plane plotted.

leads to a reduction of the streamwise Reynolds shear stress production,  $\overline{v'v'}\partial_y\overline{u}$ , which reduces the magnitude of  $\overline{u'v'}$ . Finally, this causes a reduction in the production of the TKE,  $\overline{u'v'}\partial_y\overline{u}$ , leading to the reduction in the TKE. Once the spanwise flow is sufficiently developed, the additional spanwise Reynolds shear stresses lead to additional production in the TKE, ultimately increasing it. Mechanistically, the reduction in the Reynolds shear stresses occurs because of a misalignment between the near-wall structures and those farther away from the wall leading to less efficient Reynold shear stress production (Lozano-Durán *et al.* 2020). The misalignment in the flow structures is described in more detail in § 4.4. In this section, the mechanisms described will be shown to be similar for the compressible Reynolds stresses and concludes with a description of the thermal turbulent transport.

The TKE,  $\overline{\rho k} = \overline{\rho(u''u'' + v'''v'' + w''w''')}/2$  and some representative Reynolds stresses are plotted in figure 8(a-f) for Ma=1.5 and  $\Pi=40$ . The evolution of the Reynolds stresses can be divided into two stages. The first stage is characterized by a reduction in  $\overline{\rho u''u''}$  due to decreased production from the drop in  $\overline{\rho u''v''}$ . This coincides with a reduction in  $\overline{\rho v''v''}$  due to the decrease in the production of  $\overline{\rho u''v''}$  (Moin *et al.* 1990; Lozano-Durán *et al.* 2020). While this is occurring, there is an increase in  $\overline{\rho w''w''}$  due to the net transport in the spanwise direction's role in generating  $\overline{\rho v''w''}$ , leading to production of spanwise turbulent fluctuations. Despite the increase in the mean kinetic energy and spanwise turbulent fluctuations, there is a reduction in the TKE driven by the reduction in production from  $\overline{\rho u''v''}$  in agreement with various incompressible studies with imposed spanwise flows (Bradshaw 1977; Moin *et al.* 1990; Lozano-Durán *et al.* 

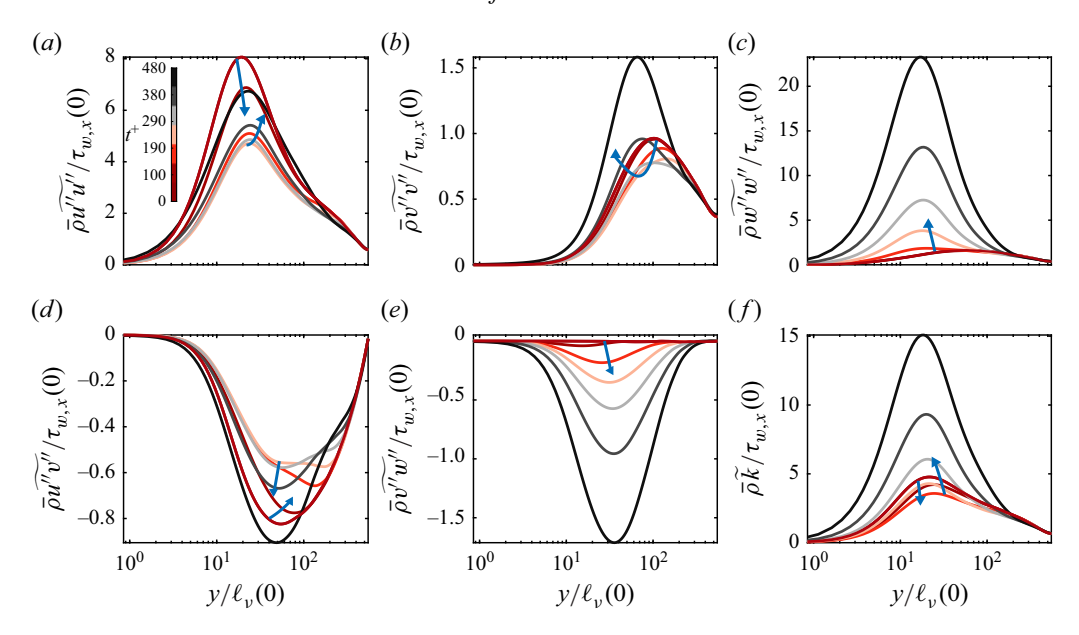


Figure 8. Temporal variation of (a-e) the Reynolds stresses and (f) TKE for Ma=1.5 and  $\Pi=40$ , normalized by the initial  $\tau_{w,x}$ . The lines are coloured with the colourbar at every  $80\ell_{\nu}(0)/u_{\tau}(0)$  in (a) and the arrows illustrate the direction of time in the statistics.

2020). During the second stage, the  $\overline{\rho}u''v''$  intensifies, leading to an increase in  $\overline{\rho}u''u''$  while  $\overline{\rho}w''w''$  continues to rise. As a result, the TKE increases at this point as well. In Gomez (2025), the  $\Pi=10$  and Ma=1.5 case was shown to follow the same trends as the  $\Pi=40$  case, although the decrease in the magnitude of  $\overline{\rho}u''v''$  was smaller, leading to a smaller reduction in the TKE. Furthermore, the TKE and Reynolds stresses of the other cases were shown to follow similar trends, with cases 1 and 2 demonstrating almost identical temporal evolution.

While the Reynolds stresses follow similar behaviour between the  $\Pi=10$  and  $\Pi=40$  cases, the velocity-temperature covariances,  $\widehat{u''T''}$ , have qualitatively different responses to the spanwise acceleration. Focusing first on the  $\Pi=10$  and Ma=1.5 case in figure 9(a-d), the covariances illustrate a slight reduction in  $\widehat{u''T''}$  and  $\widehat{v''T''}$  and an increase in  $\widehat{w''T''}$ . The latter reflects the increased transport in the spanwise direction. The slight changes in  $\widehat{u''T''}$  reflect that the u fluctuations remain correlated with the T fluctuations while the anticorrelation between v'' and T'' reflect the importance of sweep and ejection events even in the presence of spanwise acceleration. Despite the change in the magnitudes,  $\widehat{u''T''}$  and  $\widehat{v''T''}$  behave similar to canonical compressible flows (Coleman  $et\ al.\ 1995$ ). Finally,  $\widehat{T''T''}$  decreases despite the net increase in  $\widehat{T}$ , similar to the reduction in TKE.

The  $\Pi=40$  and Ma=1.5 case's velocity-temperature covariances and thermal fluctuations in figure 9(e-h), illustrate a significantly different response. For initial times,  $\widetilde{u''T''}$  and  $\widetilde{v''T''}$  decrease in magnitude while  $\widetilde{w''T''}$  increases. Eventually, the velocity-temperature covariances change signs along y at  $t^+\approx 280$ . This behaviour can be observed in the instantaneous visualizations of u' and T' in figure 7(b,d,f,h) and highlights a difference in the turbulent thermal transport absent in the  $\Pi=10$  case. These differences can be explained by comparing  $\widetilde{T}$  in figure 3. For  $\Pi=10$ ,  $\widetilde{T}$  remains monotonic in the

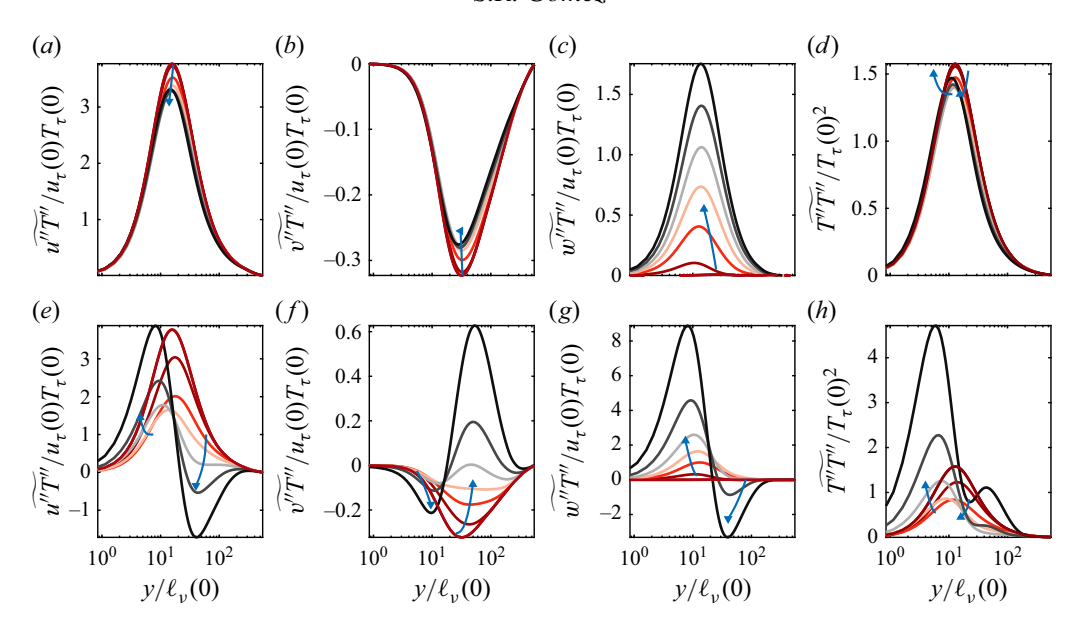


Figure 9. Temporal variation of (a-c,e-g) the velocity-temperature covariances normalized by  $u_{\tau}(0)$  and  $T_{\tau}(0)$  and

wall-normal direction, whereas for  $\Pi=40$ , a near-wall  $\widetilde{T}$  peak emerges for  $t^+\approx 200$ . Thus, for  $t\gtrapprox 200$ , the lift-up mechanisms change the transport of T' above this near-wall  $\widetilde{T}$  peak. Below this peak,  $\widetilde{u}$ ,  $\widetilde{w}$  and  $\widetilde{T}$  are all monotonically increasing like in the  $\Pi=10$  case, maintaining the same behaviour in the velocity-temperature covariances. Away from the peak,  $\widetilde{T}$  is monotonically decreasing whereas  $\widetilde{u}$  and  $\widetilde{w}$  increase in y. This means that the lift-up mechanism advects low-speed, high temperature fluid up away from the temperature peak and high-speed, low temperature fluid down towards the peak. Thus, the change in sign in  $\widetilde{u_i''}T''$  above the near-wall  $\widetilde{T}$  peaks stems from changes in the lift-up mechanism. Similar observations have been made in turbulent boundary layers (Duan et al. 2010; Pirozzoli & Bernardini 2011). In § 4.2, the lift-up mechanisms are discussed in more detail. Finally,  $\widetilde{T''}T''$  also decreases for initial times as shown in figure 9(h), similar to what happened in the  $\Pi=10$  case. For later times,  $\widetilde{T''}T''$  increases and produces two peaks likely stemming from decreased production near the zero-crossing of  $\widetilde{v''}T''$  and  $\partial_y \widetilde{T}$ .

The reduction in the TKE and  $\overline{\rho}T''T''$  can be explained by considering their budgets. First, the Reynolds stress budget is

$$\partial_t \left( \overline{\rho u_i'' u_j''} \right) = \mathcal{P}_{ij} + \mathcal{T}_{ij} + \mathcal{S}_{ij} + \mathcal{E}_{ij} + \mathcal{A}_{ij} + \mathcal{C}_{ij}$$

$$\tag{4.1}$$

where  $\mathcal{P}_{ij} = -\overline{\rho}(\widetilde{u_i''u_k''}\partial_{x_k}\widetilde{u}_j + \widetilde{u_j''u_k''}\partial_{x_k}\widetilde{u}_i)$ , is the production,  $\mathcal{T}_{ij} = -\partial_{x_k}\rho\widetilde{u_i''u_j''u_k''}$  is the turbulent transport,  $\mathcal{S}_{ij} = -(\overline{u_j''\partial_{x_i}p'} + \overline{u_i''\partial_{x_j}p'})$  is the pressure-strain,  $\mathcal{E}_{ij} = -(\overline{u_i''\partial_{x_k}\tau_{jk}'} + \overline{u_j''\partial_{x_k}\tau_{ik}'})$  is the dissipation,  $\mathcal{A}_{ij} = -\widetilde{v}\partial_y(\overline{\rho}\widetilde{u_i''u_j''})$  is the wall-normal advection and  $\mathcal{C}_{ij} = \overline{u_i''}\partial_{x_k}(\overline{\tau}_{jk} - \overline{p}\delta_{jk}) + \overline{u_j''}\partial_{x_k}(\overline{\tau}_{ik} - \overline{p}\delta_{ik})$  are the compressibility terms. The thermal

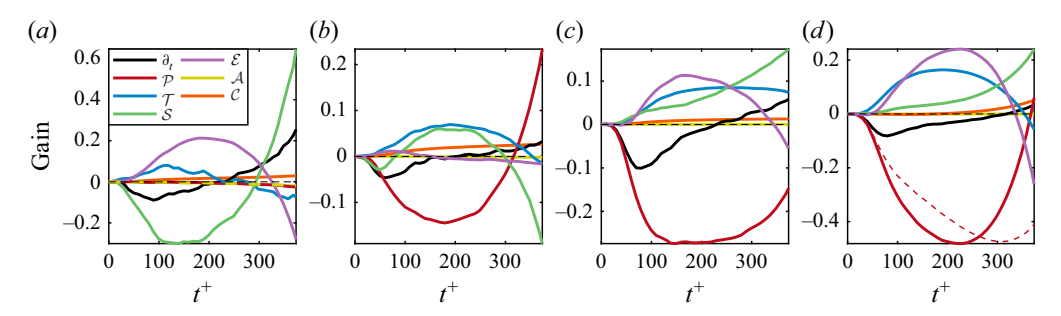


Figure 10. The gains of the  $\overline{\rho}v''v''$  (a),  $\overline{\rho}u''v''$  (b),  $\overline{\rho}u''u''$  (c) and  $\overline{\rho}T''T''$  (d) budgets integrated from  $y/\ell_v(0) \in [5,75]$  for Ma=1.5 and  $\Pi=40$ . The gains in (a) are normalized by the initial pressure-strain whereas (b) and (d) are normalized by their initial production terms. In (d), the red-dashed line is  $-2\overline{\rho}v''T''\partial_v T$ .

budget is

$$\partial_t \left( \widetilde{\rho} \widetilde{T''T''} \right) = \mathcal{P}_{TT} + \mathcal{T}_{TT} + \mathcal{S}_{TT} + \mathcal{E}_{TT} + \mathcal{A}_{TT} + \mathcal{C}_{TT}, \tag{4.2}$$

where  $S_{TT} = 2c_v^{-1}(\overline{T''S_{ij}''\tau_{ij}'} - \overline{T''\partial_{x_i}u_i''p'})$  is the thermal pressure-stress strain,  $\mathcal{P}_{TT} = 2(-\overline{\rho}\widetilde{v''T''\partial_y}\widetilde{T} - (\gamma - 1)\overline{\rho}\widetilde{T''T''\partial_y}\widetilde{v} + c_v^{-1}\overline{T''\tau_{yi}}\partial_y\widetilde{u}_i + c_v^{-1}\overline{S_{ij}''T''}(\overline{\tau}_{ij} - \overline{p}\delta_{ij}))$  is the thermal production,  $\mathcal{E}_{TT} = 2c_v^{-1}\overline{\partial_{x_i}T''q_i}$  is the heat dissipation,  $\mathcal{T}_{TT} = -\partial_y(\overline{\rho}\overline{T''T''v''}) - 2c_v^{-1}\partial_y\overline{T''q_y}$  is the turbulent and heat transport,  $C_{TT} = 2c_v^{-1}\overline{T''}\overline{\tau}_{yi}\partial_y\overline{u}_i$  is the compressibility term and  $\mathcal{A}_{TT} = \partial_y(\overline{\rho}\widetilde{v}T''T'')$  the wall-normal convection. Here,  $S_{ij} = (\partial_{x_j}u_i + \partial_{x_i}u_j)/2$  is the strain rate tensor and  $\delta_{ij}$  is the Kronecker delta. Each individual term in (4.1)–(4.2) is integrated as  $\phi_I(t) = \int_{5\ell_v(0)}^{75\ell_v(0)} \phi(y,t) dy$  with the gains computed as  $(\phi_I(t) - \phi_I(0))$  as in Lozano-Durán  $et\ al.\ (2020)$ .

The gains for  $\overline{\rho}v''v''$ ,  $\overline{\rho}u''v''$ ,  $\overline{\rho}u''v''$  and  $\overline{\rho}T''T''$  budgets are plotted in figure 10(a-d) for Ma=1.5 and  $\Pi=40$ . The temporal evolution of the Reynolds stress budgets follows the incompressible pattern (Moin *et al.* 1990; Lozano-Durán *et al.* 2020) in that a drop in  $S_{22}$  causes a reduction in  $\overline{\rho}v''v''$ . The decrease in  $\overline{\rho}v''v''$  then causes a drop in  $\mathcal{P}_{12}$  via  $\overline{\rho}v''v''\partial_y\widetilde{u}$ , which subsequently reduces  $\overline{\rho}u''v''$ . This reduction further causes a drop in  $\mathcal{P}_{11}$ , leading to a decrease in both  $\overline{\rho}u''u''$  and the TKE. The temporal evolution of the gains are similar to those reported by Lozano-Durán *et al.* (2020), including even the initial drop in  $S_{12}$  before it rises. The decrease in  $\overline{\rho}T''T''$  comes from a reduction in  $\mathcal{P}_{TT}$  despite the increase in  $\mathcal{E}_{TT}$ ,  $\mathcal{T}_{TT}$  and  $S_{TT}$  similar to what is observed in  $\overline{\rho}u''u''$ . The term most responsible for the decrease in  $\mathcal{P}_{TT}$  is the  $-2\overline{\rho}v''T''\partial_y\widetilde{T}$  term, which is analogous to the  $\overline{\rho}v''u''\partial_y\widetilde{u}$  production term in the TKE and  $\overline{\rho}u''u''$  budget.

# 4.2. Organization of turbulent and thermal transport

In § 4.1, the presence of the near-wall peak in  $\widetilde{T}$  leads to a change in sign in the velocity–temperature covariances that is only observed in the  $\Pi=40$  case. Additionally, the development of  $\widetilde{w}$  leads to the production of  $\overline{\rho}w''w''$  via the generation of  $\overline{\rho}v''w''$ . In this section, quadrant decompositions (Wallace 2016) will be used to study the organization of the turbulent and thermal transport. While the quadrant decomposition is most commonly

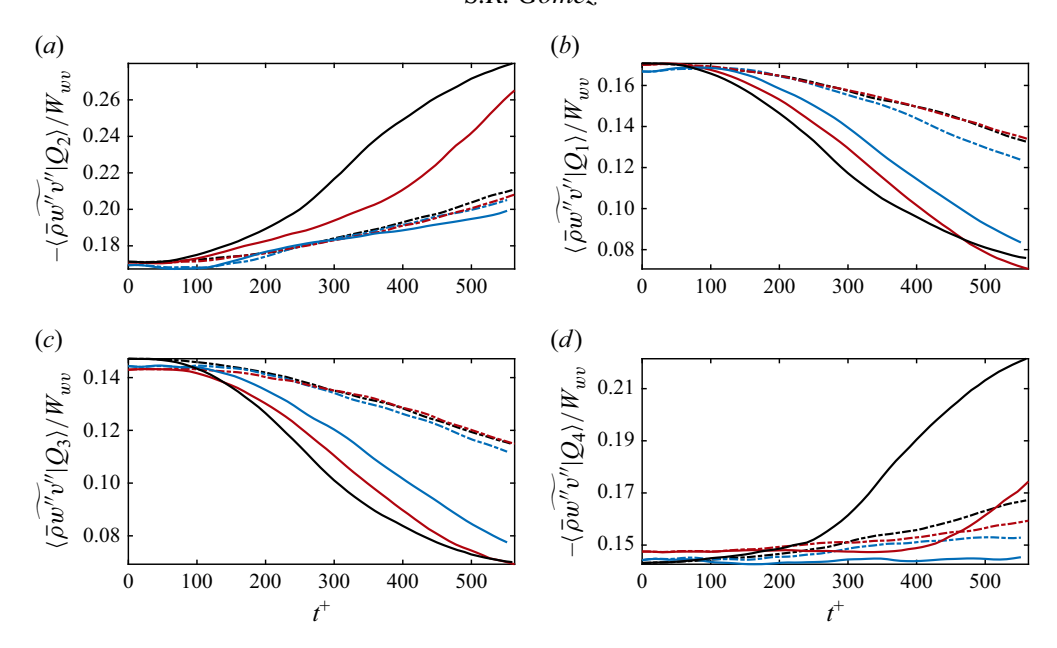


Figure 11. Temporal evolution of the (a)  $Q_2$ , (b)  $Q_1$ , (c)  $Q_3$  and (d)  $Q_4$  contributions to  $\langle \overline{\rho}w''\overline{v}'' \rangle$ , normalized by  $W_{wv}(t)$ . The colours and line styles are defined in table 1.

used to quantify contributions of u and v based on their signs (Wallace et al. 1972), the quadrant decomposition has also been used to bin T and v fluctuations (Perry & Hoffmann 1976; Nagano & Tagawa 1988; Kong et al. 2000). For a variable a and wall-normal velocity v, the quadrants are organized into four quadrants,  $Q_i$ , where  $Q_1 = \{(a, v) : a'' > 0 \text{ and } v'' > 0\}$ ,  $Q_2 = \{(a, v) : a'' < 0 \text{ and } v'' > 0\}$ ,  $Q_3 = \{(a, v) : a'' < 0 \text{ and } v'' < 0\}$  and  $Q_4 = \{(a, v) : a'' > 0 \text{ and } v'' < 0\}$ . For u, the  $Q_4$  and  $Q_2$  events are commonly denoted as sweeps and ejections, respectively. To avoid additional nomenclature, the  $Q_4$  and  $Q_2$  events for w and T will also be denoted as sweeps and ejections.

The time evolution of the probability distributions of the  $Q_i$  events was presented in Gomez (2025). Here, the contributions of the  $Q_i$  events to  $\overline{\rho}\widetilde{w''v''}$  and  $\overline{\rho}\widetilde{T''v''}$  are measured through

$$\langle \overline{\rho} a'' v'' | Q_i \rangle = \frac{1}{h} \int_0^h \overline{\rho}(\widetilde{a''v''} : (a, v) \in Q_i) dy, \tag{4.3}$$

for a = w, T where  $\sum_{i=1}^{4} \langle \overline{\rho} a'' v'' | Q_i \rangle = \langle \overline{\rho} a'' v'' \rangle$  and are normalized by  $W_{av}$  where

$$W_{av}(t)^{2} = \frac{1}{h^{2}} \int_{0}^{h} \widetilde{\rho a'' a''} dy \int_{0}^{h} \overline{\rho v'' v''} dy = \langle \overline{\rho} a'' a'' \rangle \langle \overline{\rho} v'' v'' \rangle > 0, \tag{4.4}$$

for  $a=w,\,T$ . Normalizing with  $\langle \overline{\rho}\widetilde{a''v''}\rangle$  can be problematic since at  $t=0,\,\langle \overline{\rho}\widetilde{w''v''}\rangle=0$  and for the  $\Pi=40$  cases, due to the change in sign in  $\widetilde{v''T''},\,\langle \overline{\rho}\widetilde{T''v''}\rangle$  could be zero. Additionally,  $\langle \overline{\rho}a''v''|Q_i\rangle/W_{av}(t)\in[-1,\,1]$  via the Cauchy–Schwarz inequality.

The  $Q_i$  contributions to  $\langle \overline{\rho w''v''} \rangle$  are shown in figure 11. At t=0, they all contribute roughly equal amounts since  $\langle \overline{\rho w''v''} \rangle = 0$  initially due to the lack of net transport in the spanwise direction. As the flow develops a net spanwise shear,  $\widetilde{w}_y$ , the sweeps and ejection

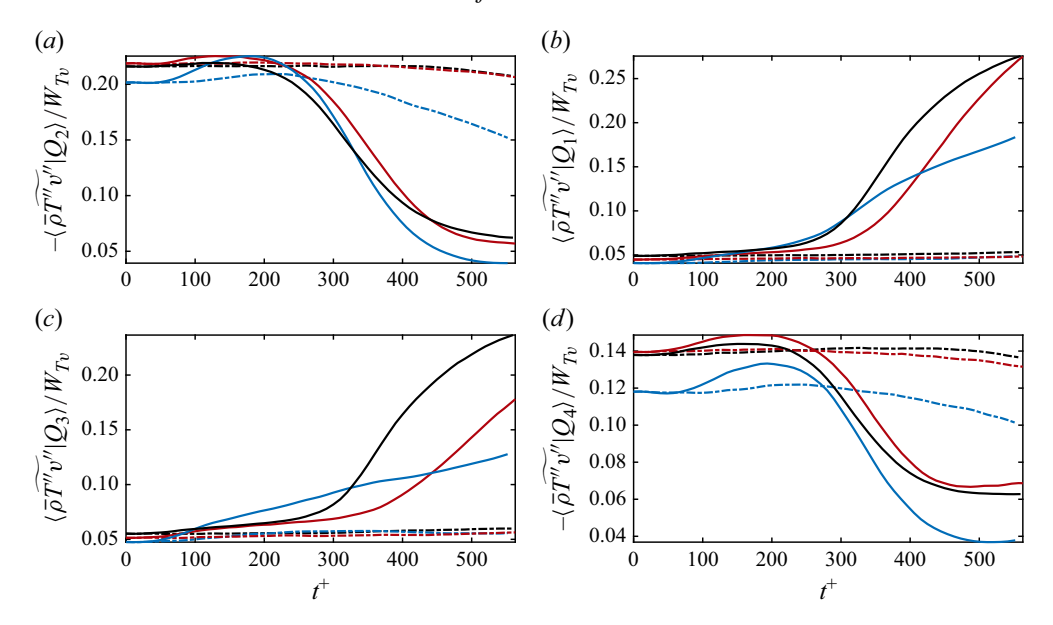


Figure 12. Temporal evolution of the (a)  $Q_2$ , (b)  $Q_1$ , (c)  $Q_3$  and (d)  $Q_4$  contributions to  $\langle \overline{\rho} T'' v'' \rangle$ , normalized by  $W_{Tv}(t)$ . The colours and line styles are defined in table 1.

events are expected to play a role via lift-up effects. Indeed, as time advances,  $Q_2$  and  $Q_4$  events play a larger role while the  $Q_1$  and  $Q_3$  become less relevant in contribution to  $\langle \overline{\rho}w''v'' \rangle$ . There is a slight preference towards ejections rather than sweeps by comparing figure 11(a,d), especially as the Ma increases.

The contributions to  $\langle \overline{\rho} \widetilde{T''v''} \rangle$  from the  $Q_i$  events are presented in figure 12. At t=0, the  $Q_2$  and  $Q_4$  contributions to  $\langle \overline{\rho} \widetilde{T''v''} \rangle$  are the most dominant, in agreement with the dominance of sweep and ejection events in the thermal transport of canonical shear flows (Perry & Hoffmann 1976; Nagano & Tagawa 1988; Kong et al. 2000). As expected from the change in sign in the velocity-temperature covariances in figure 9, the  $Q_i$  contributions reveal distinct behaviour for the  $\Pi = 10$  and  $\Pi = 40$  cases once the spanwise flow is sufficiently developed. For  $\Pi = 10$ , the  $Q_2$  and  $Q_4$  event contributions are dominant throughout the duration of the simulation, with only slight reductions in their magnitudes towards the end. The  $\Pi = 40$  cases behave similar to the  $\Pi = 10$  cases initially. For  $t^+ \approx 200$ , coinciding with the time that the near-wall  $\bar{T}$  peak emerges, the  $Q_2$  and  $Q_4$ events begin to lose their dominance while the  $Q_1$  and  $Q_3$  contributions dominate. The change from  $Q_2$  and  $Q_4$  events to  $Q_1$  and  $Q_3$  events in T support the explanation for the change in sign in the velocity-temperature covariances. That is, between the wall and the near-wall peak, the lift-up mechanism is dominated by sweeps and ejections such that  $\mp v''$  coincide with  $\pm T''$ . Between the near-wall peak and h, the sweeps and ejections are no longer dominant as  $\pm v''$  coincide with  $\pm T''$  which give rise to  $Q_1$  and  $Q_3$  events. Since the near-wall peaks occur for  $y/\ell_{\nu}(0) < 100$ , the majority of the channel is no longer governed by sweeps and ejections of T. Because of the dominance in the  $Q_1$  and  $Q_3$ events,  $\langle \overline{\rho} \widetilde{v''T''} \rangle$  changes sign in the  $\Pi = 40$  case. The trends in the  $Q_i$  events for Talign with the qualitatively different behaviour in the velocity-temperature covariances from figure 9 for the two  $\Pi$ . They further suggest that the Ma is not responsible in changing the overall organization of the turbulent-thermal transport. The observations in figure 12 agree with the results from Gomez (2025) where the contributions of the  $Q_i$ 

events were measured through the time evolution of the probabilities of the  $Q_i$  across the entire channel.

# 4.3. Temporal evolution of the wavenumber spectra

The previous sections focused on one-point statistics highlighting differences between the  $\Pi=10$  and  $\Pi=40$  cases. Here, the effects of  $\Pi$  on the turbulent structure will be further studied by comparing the temporal evolution of the spectra. While this section considers Fourier transforms along the streamwise and spanwise directions, it could be possible to define the Fourier transforms along  $e_s$  and its perpendicular,  $e_s \wedge e_y$ , or other directions defined by the flow statistics. However, the alignment of the identified structures in the next section is shown to lie between  $e_s$  and the Reynolds shear stress direction, suggesting that axes based on the turbulent statistics do not capture the alignment of the structures. Thus, for ease of interpretation and avoiding wall-normally varying axes, the Fourier transforms here are taken along the fixed streamwise and spanwise directions,  $e_x$  and  $e_z$ , respectively.

First, the streamwise Fourier modes of a variable f are defined as

$$\widehat{f}(y, t; k_x) = \frac{1}{L_z L_x} \int_0^{L_z} \int_0^{L_x} f(x, y, z, t) e^{ik_x x} dx dz, \tag{4.5}$$

averaged over the eight ensembles and over the channel half-height, where  $k_x = 2\pi/\lambda_x$  is the streamwise wavenumber and  $\lambda_x$  is the wavelength. The streamwise premultiplied power spectrum of the variable f is then  $E_{ff}(y,k_x,t) = k_x \left| \widehat{f}(y,t;k_x) \right|^2$  for  $k_x > 0$ . The spanwise premultiplied power spectrum,  $E_{ff}(y,k_z,t)$ , is defined similarly by swapping x and z using the spanwise wavenumber,  $k_z$ , and spanwise wavelength,  $\lambda_z$ .

The premultiplied kinetic energy spectra,  $E_{kk} = (E_{uu} + E_{vv} + E_{ww})/2$ , and premultiplied temperature spectra,  $E_{TT}$ , are compared for the Ma = 1.5 and  $\Pi = 40$  case in figure 13 for four representative times and the initial canonical configuration. At  $t^+ = 0$ ,  $E_{kk}(y, k_x, t)$  and  $E_{TT}(y, k_x, t)$  peak near  $(y/\ell_v(0), \lambda_x/\ell_v(0)) = (20, 1000)$  and (10, 1000), respectively, as expected for the near-wall cycle in wall-bounded turbulent flows (Lee & Moser 2015). Figure 13(a,e) reveal that the most significant initial temporal evolution in the spectra is seen in the near-wall small-scales while the spectra in the large-scale outer region mostly coincide with the canonical spectra. As time advances, the near-wall peaks move to smaller values of  $\lambda_x/\ell_v(0)$  for both  $E_{kk}$  and  $E_{TT}$ . For  $t^+ \leq 200$ , the contours for large  $\lambda_x$  away from the wall still coincide with the contours from  $t^+ = 0$ , suggesting that the effect of  $g_z$  on the large-scales lags behind its effect on the small-scales. Similar observations were made with structural observations of wall-attached Reynolds shear-stress carrying eddies in incompressible flow (Lozano-Durán *et al.* 2020) and are expanded in § 4.4. Eventually, the large-scale structures become less energetic as they too orient away from  $e_x$ .

The movement of the near-wall peak to smaller  $\lambda_x$  and y is related to two mechanisms. The first is as  $\tau_w$  increases, the viscous length scale decreases causing the characteristic size of the near-wall structures to subsequently shrink. The second is that the extent of the near-wall structures along  $e_x$  decreases as these structures turn in the direction of the net acceleration. As a result of these two mechanisms and assuming these near-wall structures have an orientation of  $\theta$ , the characteristic streamwise wavelength, l, and wall-normal location,  $y_l$ , of the structures in the near-wall peak can be approximated as

$$(l(t), y_l(t)) \approx (1000 \cos(\theta(t)), y_0) \ell_{\nu}(t),$$
 (4.6)

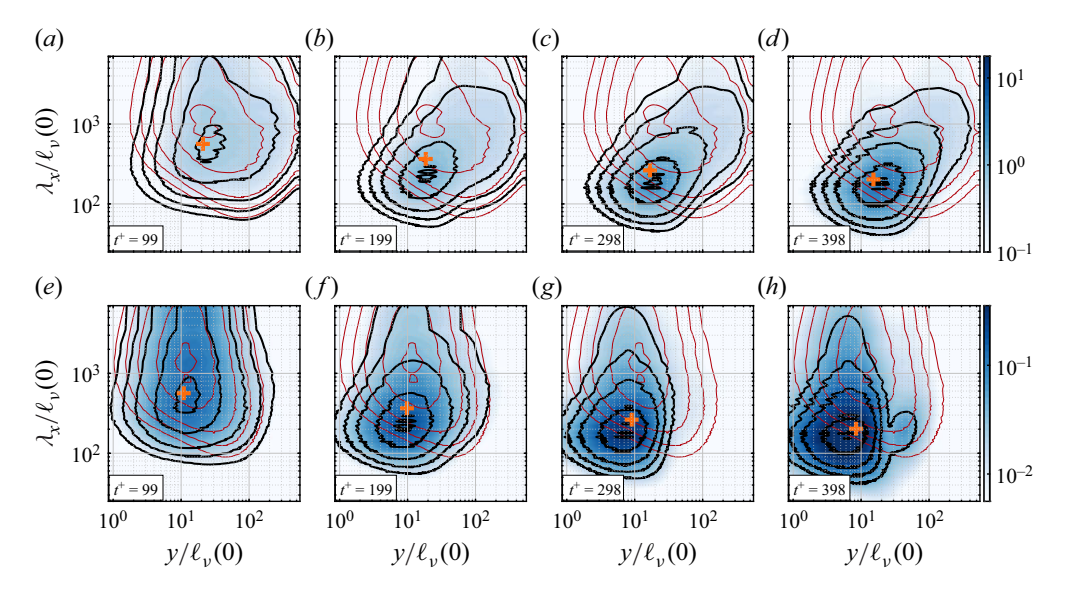


Figure 13. Instantaneous contours of the streamwise premultiplied spectra for Ma = 1.5 and  $\Pi = 40$  with  $hE_{kk}(y, k_x, t)/u_{\tau}(0)^2$  (a-d) and  $hE_{TT}(y, k_x, t)/T_{\tau}(0)^2$  (e-h). The solid lines are isocontours of 5%, 10%, 20%, 50% and 95% of the maximum instantaneous premultiplied spectra. The black solid lines and coloured contours are at the time listed while the red solid lines are taken at  $t^+ = 0$  as a comparison. The solid orange crosses denote the predicted location of the near-wall peak via (4.6).

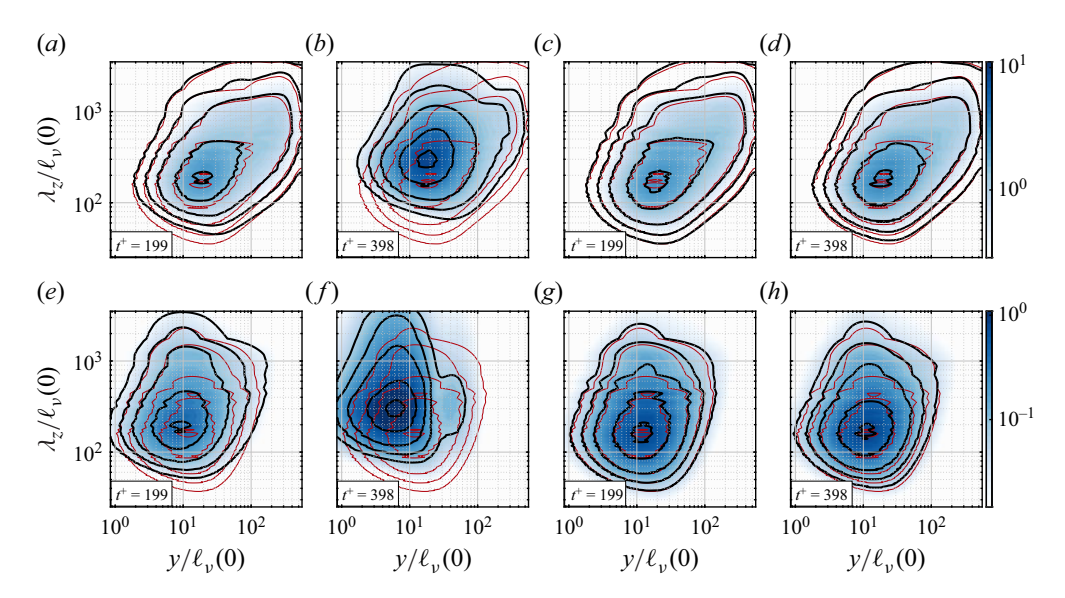


Figure 14. Similar to figure 13, except  $E_{kk}(y, k_z, t)$  (a-d) and  $E_{TT}(y, k_z, t)$  (e-h) are plotted for Ma = 1.5,  $\Pi = 40$  in (a), (b), (e) and (f) and Ma = 1.5,  $\Pi = 10$  in (c), (d), (g) and (h).

where  $y_0 = 20\ell_{\nu}(0)$  and  $10\ell_{\nu}(0)$  for  $E_{kk}(y, k_x, t)$  and  $E_{TT}(y, k_x, t)$ , respectively. These are shown to approximately fall near the location of the near-wall peaks, albeit in log-space.

The premultiplied spanwise spectra,  $E_{kk}(y, k_z, t)$  and  $E_{TT}(y, k_z, t)$ , at Ma = 1.5 are compared between the  $\Pi = 40$  case in figure 14(a,b,e,f) and the  $\Pi = 10$  case in

figure 14(c,d,g,h). At t=0, both  $E_{kk}$  and  $E_{TT}$  peak around  $y/\ell_{\nu}\approx 15$  and  $\lambda_z/\ell_{\nu}(0)\approx 200$ , which are characteristic of the near-wall cycle in both incompressible and compressible flows (Lee & Moser 2015; Cogo *et al.* 2022). Unlike the streamwise spectra,  $E_{kk}(y, k_z, t)$ , reacts slower to the spanwise acceleration such that the isocontours for up to  $t^+=199$  approximately overlap with those at  $t^+=0$  for  $\Pi=40$ . As time advances, the peak  $E_{kk}$  move to larger  $\lambda_z$  due to the increased alignment of the kinetic energy structures towards  $e_z$ . The isocontours of  $E_{TT}$  for the  $\Pi=40$  case depart from the  $t^+=0$  isocontours faster than  $E_{kk}$ . The near-wall peaks of  $E_{TT}$  move significantly closer to the wall while also moving towards larger  $\lambda_z$ . Both figures 13(h) and 14(f), reveal a secondary peak in  $E_{TT}$  of small-scales in the buffer layer away from the primary near-wall peak. This secondary peak is responsible for the secondary peak in the plots of T''T'' from figure 9(h). On the other hand, the temporal evolution in the  $\Pi=10$  case does not substantially affect the spanwise spectra. This suggests a small gradual change in the spanwise organization of the flow due to the weaker acceleration, despite the changes to the mean flow during the simulation time.

The structure of the outer-layer turbulent eddies is now studied by extending the characteristic length scale,  $\ell_{1,2}(y) \sim (u_\tau h)^{1/2} (\partial_y \overline{u})^{-1/2}$ , introduced in Pirozzoli (2012) for canonical wall-bounded flows to the compressible transient 3-D flow. The success of  $\ell_{1,2}$  is in agreement with the attached eddy model (Townsend 1976; Perry & Marusic 1995) which argues that the length scales of the turbulent eddies grow with wall-normal height. By consideration of the Ma-independence under an appropriate velocity transformation,  $\ell_{1,2}$  has been extended to compressible flows by replacing  $\partial_y \overline{u}$  in  $\ell_{1,2}$  with the appropriately transformed mean shear. Modesti & Pirozzoli (2016) used the Van Driest (1951) transformation whereas Cogo et al. (2022) noted an improvement when using the GFM transformation due to a better agreement with the incompressible flow in the mean flow field. Using the velocity transformation in (3.2), a time-dependent, compressible  $\ell_{1,2}$  is introduced as

$$\ell_{1,2}^*(y,t) = (u_{\tau}(t)h)^{1/2} \left( \frac{u_{\tau}(t)}{\ell_{\nu}(t)} \frac{\partial \|\widetilde{\boldsymbol{u}}\|_{TL}}{\partial y^*} \right)^{-1/2} = (h\ell_{\nu}(t))^{1/2} \left( \frac{\partial \|\widetilde{\boldsymbol{u}}\|_{TL}}{\partial y^*} \right)^{-1/2}. \tag{4.7}$$

Since  $\ell_{1,2}$  relied on an assumption that the outer scale is characterized by  $u_{\tau}$ , h and the local shear, it is expected then that  $\ell_{1,2}^*$  should only hold in regimes where  $u_{\tau}$ , h and the velocity transformation define a Ma- and time-independent outer region. From figure 3(d,e), this is only satisfied for the  $\Pi=10$  cases. The normalized premultiplied spanwise spectra,  $E_{kk}(y, kz, t)/k(y, t)$ , are plotted as a function of  $\lambda_z/h$  in figure 15(a–d) and a function of  $\lambda_z/\ell_{1,2}^*(y,t)$  in figure 15(e-h). For the  $\Pi=10$  cases,  $\ell_{1,2}^*(y,t)$  collapses the spectra at the different wall-normal heights by accounting for the temporal and wallnormal variation in the transport properties, further demonstrating that ideas presented in Pirozzoli (2012), Modesti & Pirozzoli (2016) and Cogo et al. (2022) extend to this 3-D transient compressible flow. Similar to Cogo et al. (2022),  $E_{TT}(y, t; k_z)$  also exhibits the same outer-layer self-similarity as a function of  $\lambda_z/\ell_{1,2}^*$  for  $\Pi=10$ , though this result is omitted for brevity. In line with the theory, the Ma = 1.5,  $\Pi = 40$  case is not able to appropriately collapse the spectra due to the time-dependence in the wake using the TL transformation. Though not shown, the other  $\Pi = 40$  cases do not admit this  $\ell_{1,2}^*$ scaling. The lack of collapse for  $\Pi = 40$  is a consequence of the strong acceleration creating non-equilibrium effects in  $\tilde{u}$  rather than compressibility effects. The success of  $\ell_{1,2}^*$  in characterizing the spanwise scales may suggest that the eddies in the  $\Pi=10$  cases evolve in quasiequilibrium whereas the eddies of the  $\Pi = 40$  cases are in non-equilibrium, using the definition of equilibrium from Lozano-Durán et al. (2020). Additionally, it

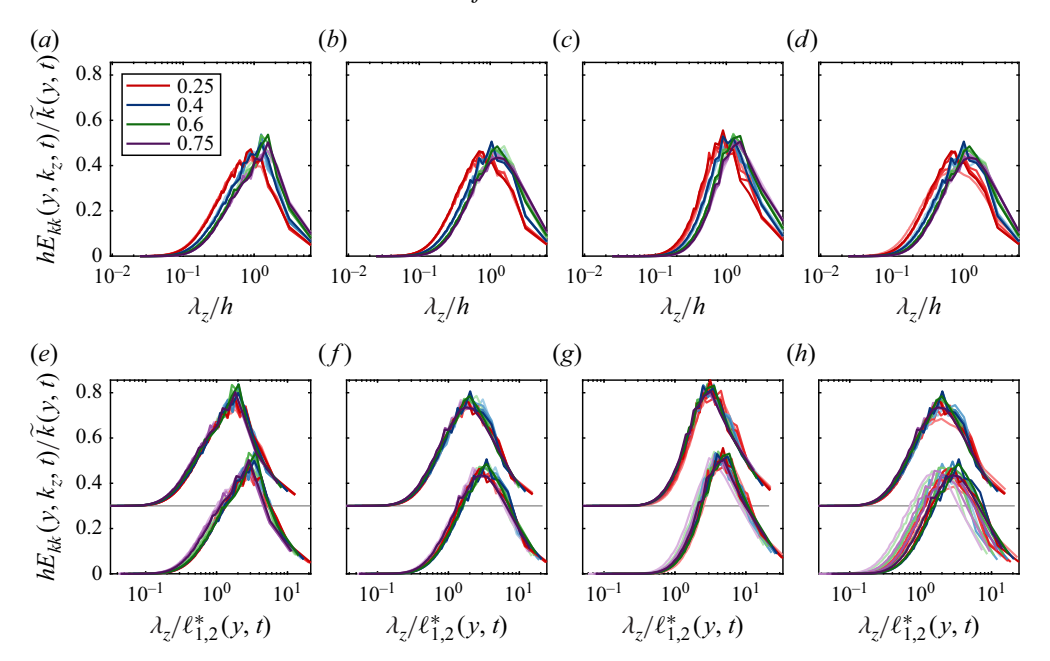


Figure 15. Normalized premultiplied spanwise spectra as a function of  $\lambda_z/h$  (a,b,c,d),  $\lambda_z/\ell_{1,2}^*(y,t)$  and  $\lambda_z/\widetilde{\ell}_{1,2}^*(y,t)$  (off-set vertically by 0.3 for visibility) (e,f,g,h) for case 1 (a,e), case 2(b,f), case 3(c,g) and case 5(d,h). The different colours denote different y/h and dark to light indicate increasing time, in increments of  $160\ell_V(0)/u_T(0)$ .

may be a consequence of a strong deviation from the log-law. To remedy this,  $\ell_{1,2}^*(y,t)$  is replaced with  $\widetilde{\ell}_{1,2}^*(y,t) = \sqrt{h\ell_\nu y^*}$  in line with the attached-eddy theory. Using this scaling in figure 15(e-h) provides an improvement for the scaling, even the  $\Pi=40$  case. Thus, despite the non-equilibrium conditions, the typical eddy size grows with the vertical distance using the semilocal coordinate as  $\sqrt{\ell_\nu y^*}$ . The success of the  $\widetilde{\ell}_{1,2}^*$  scaling highlights the delayed response in the turbulent organization in the outer region to the spanwise acceleration relative to the near-wall, as discussed in § 4.4.

## 4.4. Transport of turbulent and thermal coherent structures

Although the spectra provide insight into the structural organization of the flow, it is limited to scales defined along  $e_x$  and  $e_z$  despite the 3-D statistics. To study the organization of the turbulent eddies in an axis-free manner, the structure identification proposed by Lozano-Durán *et al.* (2012) is used. Based on the spectra in § 4.3 and previous work on the structural characteristics of 3-D boundary layers, the nearwall structures respond to the spanwise acceleration before the large-scale structures creating misalignment. This misalignment is the mechanism responsible for inhibiting the Reynolds stress production (Lozano-Durán *et al.* 2020). This conceptual picture is illustrated in figure 16(a,b) for the canonical channel at t=0 and sometime after the spanwise body force has been imposed. Here, the organization of the kinetic energy-and temperature-carrying eddies will be studied to quantify the misalignment between the near-wall and large-scale structures.

To define the kinetic energy structures, the instantaneous kinetic energy is first defined as  $K = (u^2 + v^2 + w^2)/2$  and the fluctuating kinetic energy is then  $K' = K - \overline{K}$ . The kinetic energy structures and temperature structures are defined as connected regions,  $\Omega$ ,

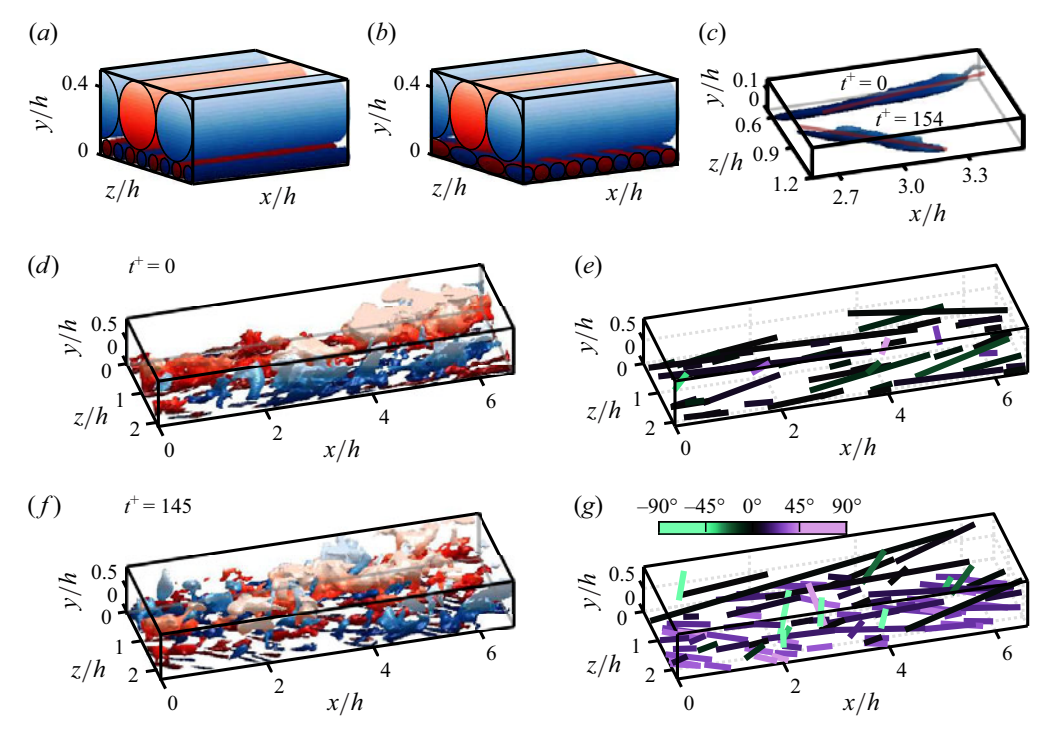


Figure 16. Cartoon of the near-wall small scale structures and large-scale structures at t=0 (a) and t>0 (b) demonstrating the faster alignment of the near-wall structures than the larger structures farther from the wall. Representative near-wall kinetic energy structures identified at  $t^+=0$  and  $t^+=145$  with their spines in red (c). Instantaneous realizations of identified kinetic energy structures ( $d_x f$ ) and their spines ( $e_x f$ ) at  $t^+=0$  ( $d_x f$ ) and  $t^+=145$  ( $f_x f$ ) for  $f_x f$  and  $f_x f$  are closer to the wall, and the blue and red denotes positive and negative fluctuations, respectively. The spines in (e) and (g) are coloured based on their angle with respect to  $e_x f$  as shown in the colourbar. Note that the figures plot a subset of the full computational domain to highlight some representative structures and their spines.

where

$$|K'| \geqslant 1.75\sqrt{\overline{K'K'}} \tag{4.8}$$

and

$$\left|T'\right| \geqslant 1.75\sqrt{\overline{T'T'}},\tag{4.9}$$

respectively. Note that because  $\overline{K} = (\overline{u_i'u_i'} + \overline{u_i}\overline{u_i})/2$ ,  $\overline{K'K'}$  is different from the TKE – it is the variance of the instantaneously fluctuating kinetic energy. The coefficient 1.75 determines the threshold size and this structure identification has been shown to be robust in response to changes in its value (Lozano-Durán *et al.* 2012). Connected regions whose volume is smaller than  $(30\ell_{\nu}(0))^3$  are rejected to avoid the accumulation of small disconnected structures. Each of the structure's sign can be computed based on the sign of K' or T' within each of the kinetic energy or temperature structures. To compute the angle of each structure, the centre of mass of each structure,  $x_m = x_m e_x + y_m e_y + z_m e_z$ , is first computed as

$$x_m V = \int_{\mathcal{O}} x \, \mathrm{d}x \, \mathrm{d}y \, \mathrm{d}z,\tag{4.10}$$

where V is the volume of each  $\Omega$ . Then, for each structure, the matrix, X is computed as

$$X_{jk}V = \int_{\Omega} (x_j - x_{j,m})(x_k - x_{k,m}) dx dy dz.$$
 (4.11)

Since, X is symmetric, it can be written in its spectral representation as  $X = \sum_{j=1}^{3} \alpha_{j} p_{j} \otimes p_{j}$  where  $\alpha_{1} \geqslant \alpha_{2} \geqslant \alpha_{3}$  and  $p_{j}$  are orthonormal eigenvectors often denoted as the principal axes. The principal direction of each structure is then  $p_{1}$ . The direction along the wall-parallel plane is  $e_{p}$ , the unit vector parallel to  $p_{1} - (p_{1} \cdot e_{y})e_{y}$ . Finally, the length of each structure is defined as  $r_{1} = \max(d) - \min(d)$ , where

$$d = [(x - x_m)\mathbf{e}_x + (z - z_m)\mathbf{e}_z] \cdot \mathbf{e}_p : (x, y, z) \in \Omega$$

$$(4.12)$$

is the wall-parallel distance of  $\Omega$  along  $e_p$ . The angle of the structure is defined as  $\theta$ , the angle between  $e_p$  and  $e_x$ , as  $\cos(\theta) = e_p \cdot e_x$ . Finally, the spines are defined as the line segment that intersects  $x_m$  parallel to  $p_1$  with a wall-parallel length of  $r_1$ .

In figure 16(c), the structure identification is illustrated for two representative nearwall kinetic energy structures at  $t^+ = 0$  and  $t^+ = 145$  for the Ma = 1.5 and  $\Pi = 40$  case. Their spines are included as well for visualization, illustrating that they can recover the statistical length of the structures and their change in orientation as the flow is sufficiently accelerated. Two snapshots at t = 0 and  $t^+ = 145$  are presented in figure 16(d,f) with the surface contours of the identified structures within a subset of the channel domain. At  $t^+=0$ , one can qualitatively note that the small-scale near-wall structures and largescale structures are aligned along the streamwise direction, like in the cartoon presented in figure 16(a). At  $t^+$  = 145, the data reflects figure 16(b) as the near-wall small-scale structures are aligning towards the spanwise direction while the large-scales are mostly streamwise aligned. Figure 16(e,g) plot the spines of each of the identified structures in figure 16(d,f), respectively, colour-coded by their angle  $\theta$ , the angle between the spine and  $e_x$ . At  $t^+ = 0$ , the spines all primarily have  $\theta \approx 0^\circ$ . There are some spines with large  $\theta$ corresponding to smaller-scale structures that are longer in their spanwise extent than their streamwise extent. Thus, the spine detection algorithm treats these structures as spanwise aligned. At  $t^+ = 145$ , the near-wall small-scale spines have  $\theta \gtrsim 45^{\circ}$  while the longer spines away from the wall's  $\theta$  reflect their streamwise alignment with smaller  $\theta$ . After a long enough time, the large-scale structures will eventually align with and equilibrate with the new direction of the flow. However, the focus of this section is on the initial period of the sudden spanwise acceleration.

To further quantify the orientation of the spines, instantaneous weighted histograms of  $y_m$  and  $\theta$ ,  $H(y_m, \theta)$ , are computed for each time instance across all 8 ensembles for each case and are weighted by the length  $r_1(y_m, \theta)$ . The weighted histograms are computed as

$$R_1 H(\theta, y_m) = \sum_{\breve{\theta} - \theta = \Delta\theta_1}^{\Delta\theta_2} \sum_{\breve{y}_m - y_m = \Delta y_{m,1}}^{\Delta y_{m,2}} r_1(\breve{y}_m, \breve{\theta}), \tag{4.13}$$

where  $R_1 = \sum_{\theta} \sum_{y_m} r_1(y_m, \theta)$  is the total length of all the structures and  $\Delta\theta_1$ ,  $\Delta\theta_2$ ,  $\Delta y_{m,1}$  and  $\Delta y_{m,2}$  denote the edges of the bins. The histograms use 22 linearly spaced bins in  $\theta \in (-20^{\circ}, 70^{\circ})$  and 16 logarithmically spaced bins in  $y_m/\ell_v(0) \in (2, 450)$ . The structures above the channel half-height are mapped to  $y_m \to 2h - y_m$  in (4.13) to take advantage of the statistical symmetry across the channel half-height. Weighing the histograms with  $r_1$  removes the influence of small-scale structures away from the wall whose alignment is poorly defined, like those pictured in figure 16(e,g). The orientation of the identified structures are also compared with the angle between two statistical quantities,

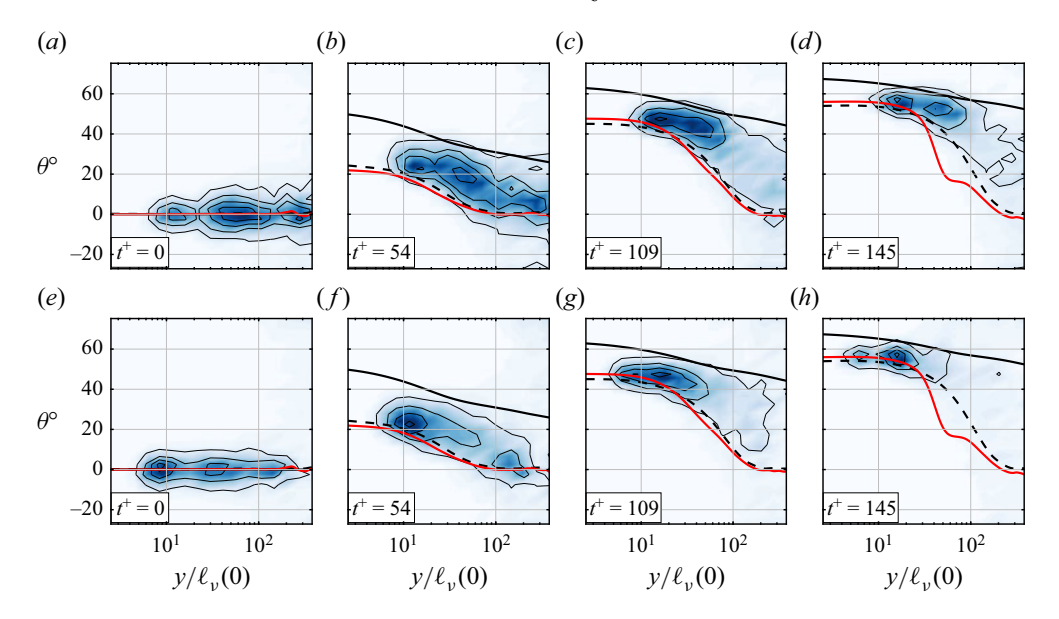
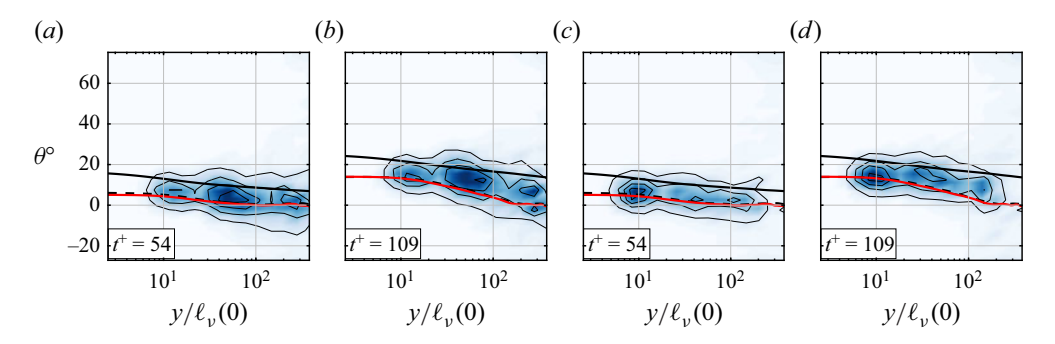


Figure 17. Weighted histogram of identified (a-d) kinetic energy structures and (e-h) temperature structures as a function of  $y_m$  and  $\theta$  for Ma=1.5 and  $\Pi=40$ . The solid black, dashed black and solid red lines denote  $\theta_{\widetilde{u},\widetilde{w}}, \theta_{\widetilde{u''v''},\widetilde{w''v''}}$  and  $\theta_{\widetilde{u''T''},\widetilde{w''T''}}$ , respectively.

 $\widetilde{a}$  and  $\widetilde{b}$ , as  $\theta_{\widetilde{a},\widetilde{b}} = \tan^{-1}(\widetilde{a}/\widetilde{b})$ , where  $\widetilde{a}$  and  $\widetilde{b}$  represent a streamwise and spanwise flow statistic, respectively. These angles are used to measure the orientation of the wall-parallel flow field,  $\theta_{\widetilde{u},\widetilde{w}}$ , the Reynolds shear stresses,  $\theta_{\widetilde{u''v''},\widetilde{w''v''}}$ , and velocity–temperature covariances,  $\theta_{\widetilde{u''T''},\widetilde{w''T''}}$ , with respect to  $e_x$ . Both  $\theta_{\widetilde{u},\widetilde{w}}$  and  $\theta_{\widetilde{u''v''},\widetilde{w''v''}}$  have been used in incompressible studies, demonstrating a lag between the mean flow field and Reynolds shear stresses (Bradshaw & Pontikos 1985; Moin  $et\ al.\ 1990$ ; Lozano-Durán  $et\ al.\ 2020$ ). The addition of  $\theta_{\widetilde{u''T''},\widetilde{w''T''}}$  serves to define a direction based on the velocity–temperature covariances.

Beginning with Ma = 1.5 and  $\Pi = 40$ , figure 17(a-d) present  $H(\theta, y_m)$  for the kinetic energy structures. As expected, the structures begin statistically likely to be streamwise aligned at t = 0 regardless of their wall-normal centroid,  $y_m$ . As evidenced by  $H(\theta, y_m)$ , the kinetic energy structures closest to the wall are the first to respond to the spanwise acceleration while the structures farther from the wall are more likely to be aligned closer to  $e_x$ . The  $H(\theta, y_m)$  of the temperature structures in figure 17(e-h) follow similar trends as the kinetic energy structures with near-wall structures more statistically likely to align in the spanwise direction. The kinetic energy and temperature structures'  $H(\theta, y_m)$  suggest that the temperature structures are more likely to be closer to the wall than the kinetic energy structures once  $g_z$  has been applied. Similar to incompressible channels, for t > 0,  $\theta_{\widetilde{u},\widetilde{w}}$  is greater than  $\theta_{\widetilde{u''v''},\widetilde{w''v''}}$  such that the direction of the Reynolds shear stresses lag compared with the direction of the mean flow field. For initial times ( $t^+ \lesssim 54$ ), both  $\theta_{\widetilde{u''v''},\widetilde{w''v''}}$  and  $\theta_{\widetilde{u''v''},\widetilde{w''v''}}$  are similar, albeit with a slight lag in the orientation of the velocity-temperature covariances' orientation with respect to the Reynolds stresses. For later times, near the wall, the  $\theta_{\widetilde{u''v''},\widetilde{w''v'''}} < \theta_{\widetilde{u'''''},\widetilde{w''''''}}$ , coinciding the the increased presence of temperature structures closer to the wall. At the same time,  $\theta_{\widetilde{u''v''},\widetilde{w''v''}}$  and  $\theta_{\widetilde{u'''v''},\widetilde{w''v''}}$  differ away from the wall as the velocity-temperature covariances change sign,



reflecting differences in the thermal fluctuation transport not reflected in the Reynolds stresses. For the times plotted here, the peaks of  $H(\theta, y_m)$  occur between  $\theta_{\widetilde{u''v''}, \overline{w''v''}}$  and  $\theta_{\widetilde{u}, \widetilde{w}}$ .

Figures 18(a,b) and 18(c,d) plot the  $H(\theta, y_m)$  of the kinetic energy and temperature structures, respectively, for Ma = 1.5 and  $\Pi = 10$  for two representative times. Similar to the  $\Pi = 40$  case, the near-wall structures align away from  $e_x$  before the outer layer structures and the temperature structures are closer to the wall than the kinetic energy structures. However, the orientation angles of  $\Pi = 10$  are much smaller while the misalignment between the near-wall and large-scale structures is less than 10° for  $\Pi = 10$  and up to 30° in  $\Pi = 40$ . Similar to the observations of Lozano-Durán *et al.* (2020), the more substantial misalignment in the strongly accelerated flow inhibits the production of  $\overline{\rho}u''v''$  and  $\overline{\rho}T''v''$  by pushing the turbulent structures out of equilibrium and creating a less efficient state for production. The success of the  $\ell_{1,2}^*$  scaling of the spectra in figure 15(e-g) for  $\Pi = 10$  suggested a quasiequilibrium state in the turbulent flow. The organization of this quasiequilibrium state reveals that the turbulent eddies are closely aligned such that the underlying turbulent structure is unchanged, consistent with the definition in Lozano-Durán *et al.* (2020).

## 5. Extension of the GRA for non-equilibrium flows

Of engineering relevance is the prediction of the mean temperature and its fluctuations. There has been a long history in relating or predicting the temperature from velocities through Reynolds analogies (Reynolds 1874; Busemann 1931; Crocco 1932; Van Driest 1951; Morkovin 1962; Walz 1962; Gaviglio 1987; Huang *et al.* 1995; Duan & Martin 2011; Zhang *et al.* 2014). However, these Reynolds analogies have only been developed for unidirectional flows, like channels and boundary layers. Here, the GRA of Zhang *et al.* (2014) is extended for 3-D, unsteady flows and tested for the six cases studied herein.

Generally, the GRA predicts  $\widetilde{T}$  and  $\widetilde{T''T''}$  from the velocity statistics, heat transfer at the wall, free stream temperature, wall temperature and fluid properties. In the channel, the free stream temperature will be replaced with  $T_c$ , the centreline temperature. The initial assumptions for the GRA, and other Reynolds analogies, begin with an assumption of steady flow for a unidirectional flow. The Reynolds analogies then assume fluctuations of either the total enthalpy or recovery enthalpy are equal to  $U_w u''$ , where  $U_w$  is a constant velocity factor. They then show that the difference between the mean recovery

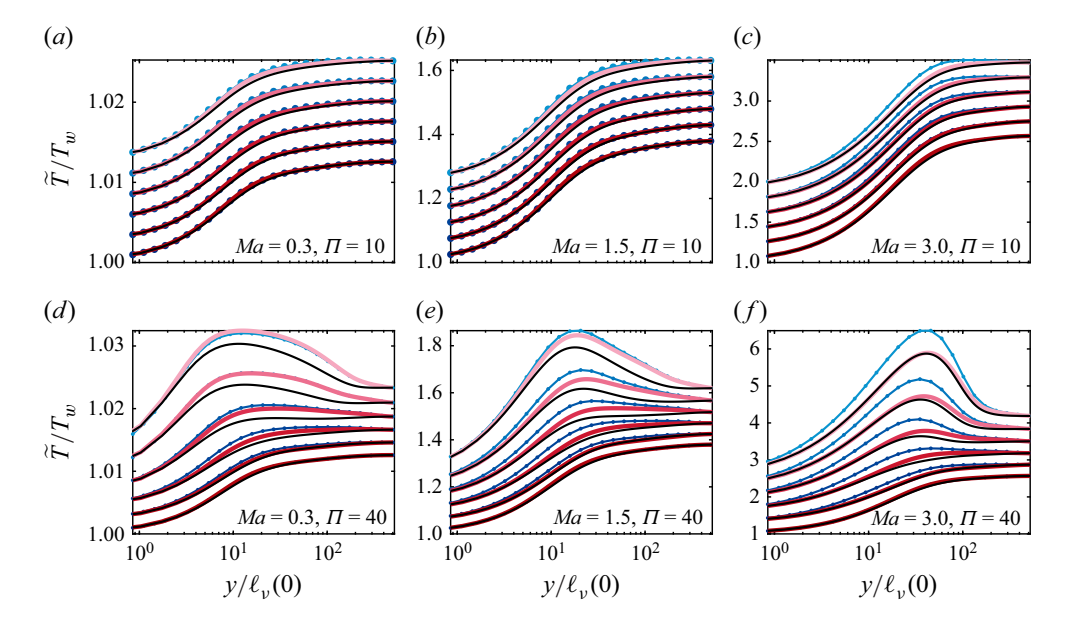


Figure 19. Prediction of  $\widetilde{T}$  from the GRA,  $T_m$ , (red thick lines),  $\widetilde{T}$  (black) and  $T_m$  computed with a constant  $r_g$  (blue dotted lines) normalized by  $T_w$  with the Ma and  $\Pi$  labelled in each plot. Lines are offset vertically and plotted in increments of  $\Delta t^+ = 100$ .

enthalpy and  $U_w\widetilde{u}$  is constant. From this relationship, the modelled temperature,  $T_m$ , can be recovered as a quadratic polynomial of  $\widetilde{u}$ . In Appendix A, it is shown that a transient and 3-D flow with a similar Reynolds analogy between the enthalpy and u'' results in a constant difference between a recovery enthalpy and  $U_w \cdot \widetilde{u}$ . Hence, the mean temperature can be modelled as a quadratic polynomial in  $\|\widetilde{u}\|$  as well. The modelled mean temperature is then

$$\frac{T_m(\|\widetilde{\boldsymbol{u}}\|, \tau_w, q_w, \beta)}{T_w} = 1 + \frac{T_{rg} - T_w}{T_w} \left( \frac{\|\widetilde{\boldsymbol{u}}\| \cos(\beta)}{\|\widetilde{\boldsymbol{u}}\|_c \cos(\beta_c)} \right) + \frac{\overline{T}_c - T_{rg}}{T_w} \left( \frac{\|\widetilde{\boldsymbol{u}}\|}{\|\widetilde{\boldsymbol{u}}\|_c} \right)^2, \quad (5.1)$$

where the subscript c is evaluated at the centreline,  $T_{rg}$  is the recovery temperature and  $\beta$  is the angle between  $\boldsymbol{u}$  and  $\boldsymbol{\tau}_w$  such that  $\cos(\beta) = \boldsymbol{e}_s \cdot \boldsymbol{e}_{s,w}$ . The recovery temperature depends on thermal transport properties, heat transfer, centreline velocity and wall shear stress as

$$T_{rg}(\|\widetilde{\boldsymbol{u}}\|, \tau_w, q_w, \beta_c) = T_c + \left(\frac{T_w - T_c}{\|\widetilde{\boldsymbol{u}}\|_c^2 / 2c_p} - \frac{2Prq_w \cos(\beta_c)}{\|\widetilde{\boldsymbol{u}}\|_c \tau_w}\right) \frac{\|\widetilde{\boldsymbol{u}}\|_c^2}{2c_p} = T_w - \frac{Prq_w \|\widetilde{\boldsymbol{u}}\|_c \cos(\beta_c)}{\tau_w c_p},$$
(5.2)

where the quantity in parenthesis is often referred to as the recovery factor,  $r_g(t)$  (Zhang *et al.* 2014). If the flow is unidirectional, (5.1) reduces to the GRA of Zhang *et al.* (2014). Here  $T_m$  accounts for the 3-D flow by incorporating the misalignment between  $\tilde{u}$  and  $\tau_w$  as well as the velocity magnitude.

A comparison between  $T_m$  and  $\widetilde{T}$  is shown in figure 19 for all six cases. Additionally,  $T_m$  where  $r_g$  is set to  $r_g(0)$  is included to consider the importance of modelling  $r_g(t)$ . The  $\Pi=10$  cases in figure 19(a-c) demonstrate the best agreement between the model and  $\widetilde{T}$ . Although the temporal evolution of  $\widetilde{T}$  was small for  $\Pi=10$ , the GRA is able to account for the significant changes in  $\widetilde{\boldsymbol{u}}$  in the prediction of  $\widetilde{T}$ . For  $\Pi=40$  in figure 19(d-f), there are discrepancies between  $T_m$  and  $\widetilde{T}$ , primarily for Ma=0.3 and Ma=1.5, though  $T_m$  is

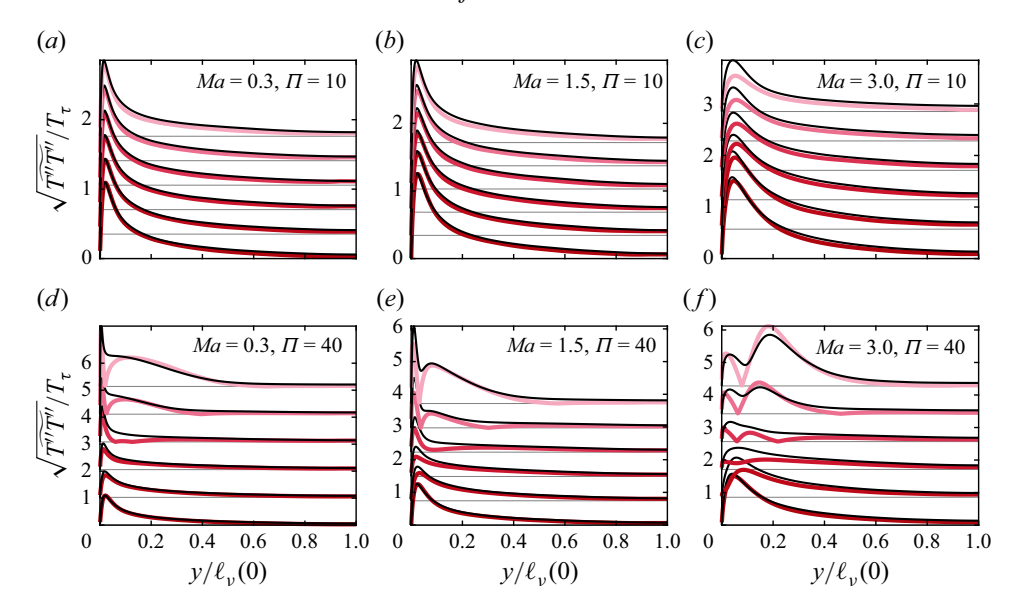


Figure 20. Prediction of  $\widetilde{T''T''}$  from the GRA (red dotted lines) and  $\widetilde{T''T''}$  (black) normalized by  $T_{\tau}(0)$  with the Ma and  $\Pi$  labelled in each plot. Here, y is normalized by h to visualize the outer region. Each line is an increment of  $\Delta t^+ = 100$  with a vertical offset denoted by the horizontal grey lines for visibility.

able to capture the near-wall  $\widetilde{T}$  peaks that emerge. The constant  $r_g$  prediction is similar to  $T_m$  for Ma=0.3 and 1.5 but over predicts in case 6. This suggests that a constant  $r_g$  can provide a useful prediction of  $\widetilde{T}$  in a 3-D transient flow if the spanwise acceleration and Ma are small.

In Appendix A, similar arguments from the GRA are used to create a model for the thermal fluctuations in the spanwise accelerating flow. The thermal fluctuations are modelled as

$$\widetilde{T''T''}_{m} = \left(\frac{\widetilde{v''T''}}{e_{i}v''u_{i}''}\right)^{2} (\widetilde{e_{i}u_{i}''})^{2}, \tag{5.3}$$

relating T''T'' to the fluctuating velocity along  $e_s$ . The term inside the parenthesis is similar to what appears in unidirectional flows, except the Reynolds shear stresses are taken along  $e_s$ . For a streamwise-aligned flow, this reduces to  $T''T''_m = (\widetilde{v''}T''/v''\widetilde{u}'')^2\widetilde{u''u''}$ .

In figure 20,  $\widetilde{T''T''}_m$  and  $\widetilde{T''T''}$  are compared for all six cases. The model and data agree throughout the channel for  $\Pi=10$  and Ma=0.3 and 1.5. The Ma=3.0 case underpredicts the near-wall  $\widetilde{T''T''}$  peak, though the outer region is well predicted. For  $\Pi=40$  in figure 20(d-f), significant disagreements emerge in the near-wall region. Namely,  $\widetilde{T''T''}_m\approx 0$  near the zero-crossing in  $\widetilde{v''T''}$ . These discrepancies arise from a lack of correlation between  $\widetilde{v''T''}$  and  $e_i\widetilde{v''u''}_i$  in the presence of strong spanwise acceleration. In the outer region of the flow, both  $\widetilde{T''T''}_m$  and  $\widetilde{T''T''}$  agree since  $\widetilde{v''T''}$  and  $e_i\widetilde{v''u''}_i$  are well correlated. Future work will need to address the lack of correlation between the Reynolds shear stresses and  $\widetilde{v''T''}$  as improvements to the GRA predictions. These are particularly

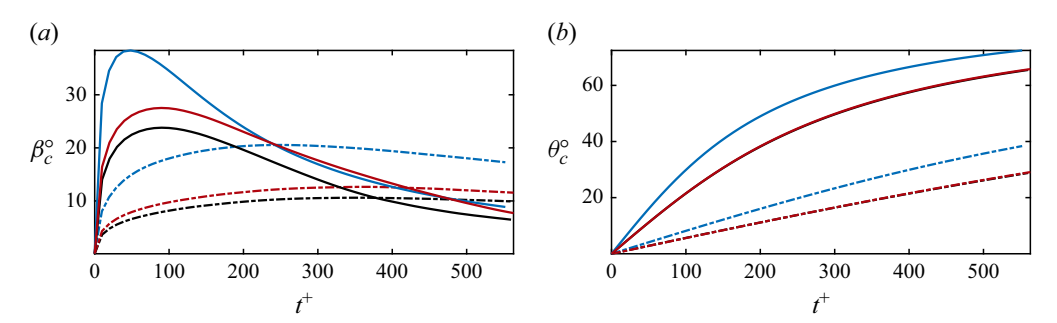


Figure 21. Measures of the sweep angle via  $\beta_c$ , the angle of the centreline velocity relative to the angle of the wall shear stress (a) and  $\theta_c$ , the angle of the centreline velocity (b) against  $t^+$  in degrees. The colours and line symbols are denoted in table 1. Note that in (b), the lines corresponding to Ma = 0.3 are just underneath the lines for Ma = 1.5.

important when changes in sign are present in the velocity-temperature covariances, even in unidirectional flows.

### 5.1. Discussion

The two choices of  $\Pi$  create two qualitatively distinct responses to the spanwise acceleration despite the Ma. These effects are primarily observed in the temperature field where a secondary peak in  $\widetilde{T}$  emerges for  $\Pi=40$  that is not observed in the  $\Pi=10$  cases. This is indicative of increased viscous heating from increased turbulent intensity. The nearwall  $\widetilde{T}$  peak is also associated with an increased  $q_w$  for the  $\Pi=40$  cases compared with the  $\Pi=10$  cases. Furthermore, the presence of the near-wall  $\widetilde{T}$  peak changes the turbulent transport of temperature fluctuations by creating a change in sign across the peak in the velocity-temperature variances and an increased contribution of  $Q_1$  and  $Q_3$  in  $\widetilde{T''v''}$ . This change in sign is not reflected in the Reynolds shear stresses, making  $\widetilde{u''v''}$  and  $\widetilde{T''v''}$  uncorrelated, which ultimately limits the predictive capabilities of the GRA. Despite their differences, both the  $\Pi=10$  and  $\Pi=40$  cases observed a decrease in  $\widetilde{T''T''}$  across the channel for early times despite the net increase in  $\widetilde{T}$ .

If the angle of  $u_c$  relative to  $\tau_w(\beta)$  is taken as a measure for the sweep angle, the sweep angles are at their peak, above 20° for  $\Pi = 40$ . Taking instead the relative velocity of  $u_c$ to  $e_x$  as the sweep angle gives, for the largest  $\Pi$ , sweep angles around  $60^{\circ}$  at the end of the simulation time. These sweep angles, plotted in figure 21, are similar to the sweep angles of supersonic aircraft, such as  $\Lambda = 55^{\circ}$  for Concorde. However, the acceleration is much different in the case of the aircraft as opposed to the ones shown herein. Using Concorde as an example once again, its spanwise acceleration can be estimated as  $(U_{\infty} \sin(\Lambda))^2/L_c$ (Vos & Farokhi 2015), where the cruising velocity is  $U_{\infty} \approx 600 \text{ m s}^{-1}$  and the chord is  $L_c \approx 20 \text{ m}$ . This will be normalized with  $a_w^2/\delta$ , where the boundary layer thickness,  $\delta$ , is estimated as  $\delta \approx 0.1$  m using a 1/5 power-law estimate (Schlichting & Gersten 2016). Concorde's normalized acceleration is then  $A_a = U_{\infty}^2 \sin(\Lambda)^2 \delta / L_c a_w^2 \approx 1.2 \times 10^{-2}$ . The normalized acceleration can also be calculated for the channel as  $A_c = g_z h/a_w^2$ . For the  $\Pi = 10$  cases used herein, the normalized acceleration is  $A_c \approx 2.5 \times 10^{-3}$ ,  $6.9 \times 10^{-2}$  and  $3.3 \times 10^{-1}$  for Ma = 0.3, 1.5 and 3.0, respectively. Thus, for similar Ma as the Concord, case 2 would be at a similar normalized spanwise acceleration as those expected from real operations. Both  $T_m$  and  $T''T''_m$  showed the best predictive capability for  $\Pi = 10$ , suggesting that these approaches may have applicability in realistic conditions.

The success of  $\widetilde{T}$  can help the development of wall models in non-equilibrium conditions. In Griffin *et al.* (2023), the GRA of Zhang *et al.* (2014) and GFM velocity transformation were combined to develop a wall-model for supersonic flows. The extensions to the TL velocity transformation in § 3.1 and the GRA may also show promise in predicting  $\widetilde{u}$  and  $\widetilde{T}$  in 3-D non-equilibrium conditions. A challenge for a wall-model of this type is that the self-similarity only extends to the viscous sublayer for large spanwise acceleration which can limit grid-size requirements. As a possible remedy for this, the Lagrangian relaxation towards equilibrium plus laminar non-equilibrium wall model (Fowler, Zaki & Meneveau 2022) can show some promise by treating the equilibrium and non-equilibrium effects separately. Future work will use the DNS data along with extensions to these models in pursuit of wall-models for non-equilibrium compressible flow.

## 6. Conclusion

While the use of a compressible flow enables the study of the heat transfer and temperature responses to spanwise acceleration, the velocity response in the compressible flow is qualitatively similar to that of the incompressible spanwise response (Moin *et al.* 1990; Lozano-Durán *et al.* 2020). By properly accounting for the property variations and new flow direction, the TL velocity transformation is able to collapse the mean velocity in the viscous sublayer. Velocity transformations were also illustrated in the similarity variable for the spanwise flow, whereby introducing the similarity variable  $\eta$  the spanwise compressible mean momentum equation could be transformed into the same similarity equation for the incompressible flow. The similarity solution for  $\widetilde{w}$  held for short times, until  $\overline{\rho} w'' v''$  became non-negligible. From this similarity solution,  $\tau_{w,z}$  could also be predicted for short times.

The turbulent fluctuations were also qualitatively similar to the incompressible regime. Both the incompressible and compressible flows observe an initial decrease in  $\overline{\rho}u''v''$  leading to a reduction in  $\overline{\rho}u''u''$  and thus a reduction in  $\overline{\rho}k''$ . While this is occurring,  $\overline{\rho}w''v''$  increases in magnitude leading to an increase in  $\overline{\rho}w''w''$  and eventually, an increase in  $\overline{\rho}k''$ . The  $\overline{\rho}u''u''$  and  $\overline{\rho}T''T''$  revealed analogous mechanisms, with the reduction in  $\overline{\rho}T''T''$  stemming from a decrease in production as well.

The temperature response depends on the strength of the spanwise acceleration. For  $\Pi=10$ , T varies little and remains monotonic in y, though there is a slight increase in overall temperature. For  $\Pi=40$ , T rises substantially along with the emergence of a near-wall peak. Despite the different responses, there is near-wall collapse of T when rescaled using the friction temperature,  $T_{\tau}(t)$ , and viscous length,  $\ell_{\nu}(t)$ , which both account for the new direction of  $\tau_{w}$ . Due to the presence of the near-wall peak, the turbulent transport of thermal fluctuations fundamentally changes. This manifests itself as a change in sign in the velocity-temperature covariances for  $\Pi=40$  while for  $\Pi=10$ , their signs remain unchanged. Additionally, for  $\Pi=40$ , the non-monotonic T presents an increase in  $Q_1$  and  $Q_3$  and decrease in  $Q_2$  and  $Q_4$  events in the thermal transport not seen in  $\Pi=10$ . These observations hint at different transport mechanisms between the thermal and momentum fluctuations away from the wall. Similar to the drop in kinetic energy, the thermal fluctuations were shown to decrease before eventually increasing. This reduction stems from an initial decrease in the thermal production of the  $\overline{\rho}T''T''$  budgets.

As the flow is accelerated for  $\Pi = 40$ , the spectra reveal that the energetic near-wall structures move closer to the wall and their streamwise extent shrinks due to their change in orientation. The spanwise size of these structures increases as the flow moves

primarily to the spanwise direction. Between the kinetic energy-carrying structures and the temperature-carrying structures, the latter move closer to the wall as  $\tau_w$  increases. The  $\Pi=10$  cases were shown to evolve in quasiequilibrium due to the collapse of the spanwise premultiplied spectra when normalized with  $\ell_{1,2}^*(t)$ . When normalized with  $\ell_{1,2}^*$ , the spectra in the  $\Pi=10$  and 40 cases also collapsed providing evidence of the attached eddy hypothesis even in non-equilibrium conditions. The orientation of the turbulent eddies was quantified with structure identification showing that the near-wall and large-scale structures are misaligned, with the former aligning in the direction of the flow first. This misalignment was severe for the  $\Pi=40$  case, possibly hinting at how this non-equilibrium state in the turbulent eddies significantly reduces the production of  $\overline{\rho}u''v''$ .

The GRA was shown to extend to statistically 3D transient flows, provided that the mean velocity's three-dimensionality is accounted for via the velocity magnitude and angle between  $\tau_w$  and  $\widetilde{u}$ .  $T_m$  agreed well for both the  $\Pi=10$  and  $\Pi=40$  cases, though discrepancies were observed in the latter. A simplified  $T_m$  with a constant  $r_g$  showed promise in predicting  $\widetilde{T}$  without the need for  $q_w$ . For  $\Pi=10$ , the modelled  $\widetilde{T''T''}$  agrees well for Ma=0.3 and 1.5. For  $\Pi=40$ , the change in sign in  $\widetilde{v''T''}$  that is not present in  $\widetilde{u_i''v''}e_i$  limits the predictions of  $\widetilde{T''T''}$  in the near-wall region since the GRA assumes  $\widetilde{v''T''}$  and  $\widetilde{u_i''v''}e_i$  are correlated. Future work will need to account for this lack of correlation to account for the zero-crossings in  $\widetilde{v''T''}$  to improve the model for  $\widetilde{T''T''}$ .

This flow introduces spanwise flow via a transient response to a strong, suddenly applied spanwise body force. In the case of swept wings, the spanwise flow occurs because of changes in geometry where spanwise pressure gradients cause the flow to accelerate. From estimates of real supersonic aircraft with swept wings, it can be argued that the spanwise pressure gradients are on a similar order of magnitude as the acceleration from the  $\Pi=10$ , Ma=1.5 case, when normalized with the speed of sound and boundary layer thickness. Thus, one may expect that the observations from the  $\Pi=10$ , Ma=1.5 case may extend to realistic aircraft design, provided that these observations hold for large  $Re_{\tau}$ .

**Acknowledgements.** S.R.G. thanks C.T. Williams and Professor P. Moin for insightful discussions and acknowledge the use of computational resources from Lawrence Livermore National Laboratory, which were instrumental in this work.

**Funding.** Funding from the Center for Turbulence Research postdoctoral fellowship and support from the Office of Naval Research through grant N000142312833 is gratefully acknowledged.

**Declaration of interests.** The author reports no conflict of interest.

## Appendix A. Derivation of GRA for transient, 3-D flows

The derivation follows similar assumptions to Zhange *et al.* (2014) except, the averaged quantities are functions of x and y rather than x and y. This derivation assumes negligible density and viscosity fluctuations such that  $\widetilde{f} \approx \overline{f}$ ,  $\overline{t}_{ij} \approx \overline{\mu}(\partial_{x_i}\widetilde{u}_j + \partial_{x_j}\widetilde{u}_i)$  and  $\overline{q}_y \approx -c_p \partial_y \widetilde{h}_e/Pr$ , where  $h_e = c_p T$  is the enthalpy and  $\widetilde{v} \ll \widetilde{u}$ . Finally, the kinetic energy is approximated as  $u_i u_i/2 \approx \widetilde{u}_i \widetilde{u}_i/2 + \widetilde{u}_i u_i''$  because mean kinetic energy is large relative to the TKE. It is convenient to work with the total enthalpy,  $H = h_e + u^2/2$  and total stress,  $\overline{t}_{T,ij} = \overline{t}_{ij} - \overline{\rho} \widetilde{u}_i'' u_i''$ . The Reynolds averaged momentum and total enthalpy equations are

$$\overline{\rho}\mathcal{D}_t \widetilde{u}_i = \partial_y (\overline{\mu}\partial_y \widetilde{u}_i - \overline{\rho}\widetilde{u}_i''v'') + \overline{\rho}g_i, \tag{A1}$$

$$\overline{\rho} \mathcal{D}_t \widetilde{H} = \partial_y (\overline{\mu} \widetilde{u}_i \partial_y \widetilde{u}_i - \overline{\rho} \widetilde{H''v''}) + \overline{\rho} g_i \widetilde{u}_i + \partial_t \widetilde{p}, \tag{A2}$$

where  $\mathcal{D}_t = \partial_t + \widetilde{v}\partial_y$ .

The GRA of Zhang *et al.* (2014) is based on extensions of the Crocco–Buseman relationship (Busemann 1931; Crocco 1932) and strong Reynolds analogies (Morkovin 1962) to  $Pr \neq 1$  through a recovery enthalpy,  $H_g = h_e + r_g u_i u_i/2$  where  $r_g$  is a recovery factor. Similar to the GRA, it is assumed that

$$\widetilde{H}_{g} + \widetilde{H}_{w} = U_{w,i}\widetilde{u}_{i}, \tag{A3}$$

$$H_g'' + c_p \phi'' = U_{w,i} u_i'', \tag{A4}$$

for some to be determined wall velocity,  $U_{w,i}$ , temperature difference,  $\phi$ , and constant wall enthalpy,  $H_w$ . It is assumed that  $U_{w,i}$  is quasisteady in time, similar to how it is considered quasiparallel in a turbulent boundary layer.

Manipulation of  $H_g$  and (A3) and (A4) identifies the following relationships:

$$\widetilde{H} = \widetilde{H}_g + (1 - r_g)\widetilde{u}_i\widetilde{u}_i/2,\tag{A5}$$

$$\overline{\mu}\widetilde{u}_{i}\widetilde{u}_{i}\partial_{y}r_{g} = (U_{w,i} - r_{g}\widetilde{u}_{i})\overline{\tau}_{i,y} + Pr\overline{q}_{y}, \tag{A6}$$

$$\widetilde{\overline{\rho}v''H''} = \widetilde{\overline{\rho}v''H_g''} + (1 - r_g)\widetilde{u}_i\overline{\rho}u_i''v'', \tag{A7}$$

$$\overline{\rho}\widetilde{v''h''_e} = (U_{w,i} - r_g\widetilde{u}_i)\overline{\rho}\widetilde{u''_i}v'' - \overline{\rho}c_p\widetilde{\phi''v''}, \tag{A8}$$

$$\overline{\mu}\widetilde{u}_{i}\partial_{\nu}\widetilde{u}_{i} = \overline{\mu}\partial_{\nu}\widetilde{H}_{g} - \overline{\mu}\partial_{\nu}\widetilde{h}_{e} + \overline{\mu}\partial_{\nu}((1 - r_{g})\widetilde{u}_{i}\widetilde{u}_{i}/2). \tag{A9}$$

An equation for the evolution of  $\widetilde{H}_g$  can be found by combining (A5), (A9) and (A7) into (A2) as

$$\overline{\rho}\mathcal{D}_t \widetilde{H}_g = \partial_y \left[ \overline{\mu} \partial_y \widetilde{H}_g - \overline{\rho} \widetilde{v''} \widetilde{H}_g'' \right] + \overline{\rho} g_i \widetilde{u}_i + \partial_t \overline{p} + R_g, \tag{A10}$$

$$R_g = \overline{\rho} \mathcal{D}_t \left[ (r_g - 1) \widetilde{u}_i \widetilde{u}_i / 2 \right] - \partial_y \left[ (r_g - 1) \overline{\tau}_{T,i} \widetilde{u}_i + (1 - Pr) \overline{q}_y + \overline{\mu} \widetilde{u}_i \widetilde{u}_i \partial_y r_g / 2 \right]. \tag{A11}$$

By applying  $\widetilde{\overline{\rho}}(\partial_t + \widetilde{v}\partial_v)$  to (A3) and using (A1), an expression for  $\widetilde{h}_e$  is found as

$$\overline{\rho} \mathcal{D}_t \widetilde{h}_e = \overline{\rho} \mathcal{D}_t ((1 - r_g) \widetilde{u}_i \widetilde{u}_i / 2) + \overline{\rho} g_i (U_{w,i} - \overline{u}_i) + (U_{w,i} - \widetilde{u}_i) \partial_v \overline{\tau}_{T,i}. \tag{A12}$$

Subtracting  $\widetilde{u}_i$  times (A1) from (A2) and using (A8) provides an alternate expression for  $\widetilde{h}_a$  as

$$\overline{\rho}\mathcal{D}_{t}\widetilde{h}_{e} = \partial_{t}\widetilde{p} + \overline{\tau}_{T,i}\partial_{\nu}\widetilde{u}_{i} - \overline{\rho}\widetilde{v''u_{i}''}\partial_{\nu}(U_{w,i} - r_{g}\widetilde{u}_{i}) - c_{p}\overline{\rho}\widetilde{v''\phi''} - c_{p}\overline{\mu}\partial_{\nu}\widetilde{T}/Pr. \quad (A13)$$

From (A12) and (A13), an expression for the recovery kinetic energy emerges as

$$\overline{\rho}\mathcal{D}_{t}((r_{g}-1)\widetilde{u}_{i}\widetilde{u}_{i}/2) = \partial_{y}\left(\left(U_{w,i} - r_{g}\widetilde{u}_{i}\right)\overline{\rho}\widetilde{v''u_{i}''} - c_{p}\overline{\rho}\widetilde{v''\phi''} + c_{p}\overline{\mu}\partial_{y}\widetilde{T}/Pr\right) + \overline{\rho}g_{i}(U_{w,i} - \widetilde{u}_{i}) + U_{w,i}\partial_{y}\overline{\tau}_{T,i} - \partial_{y}(\widetilde{u}_{i}\overline{\tau}_{T,i}) + \partial_{t}\overline{\rho}.$$
(A14)

Equations (A14) and (A6) are then used to simplify (A11) as

$$R_g = -c_p \partial_y \left( \overline{\rho} \widetilde{v''} \phi'' \right) + \overline{\rho} g_i (U_{w,i} - \widetilde{u}_i) - \partial_t \widetilde{p}. \tag{A15}$$

With the simplified expression of  $R_g$  and (A4), (A10) can be simplified as

$$\overline{\rho} \mathcal{D}_t \widetilde{H}_g = \partial_y \left( \overline{\mu} \partial_y \widetilde{H}_g - \overline{\rho} U_{w,i} v^{"u}_i'' \right). \tag{A16}$$

Subtracting this expression from the product of  $U_{w,i}$  and (A1), reveals that

$$(\overline{\rho}\mathcal{D}_t - \partial_v(\overline{\mu}\partial_v))(\widetilde{H}_g - U_{w,i}\widetilde{u}_i) = 0$$
(A17)

which confirms (A2).

To determine  $U_{w,i}$ , the dot product  $U_{w,i}\widetilde{u}_i$  is rewritten as  $\|U_w\|\|\widetilde{u}\|\cos(\beta)$ , where  $\beta$  is the angle between  $U_w$  and  $\widetilde{u}$  and  $\widetilde{u}_i\widetilde{u}_i$  as  $\|\widetilde{u}\|^2$ . Using these expressions, (A2) is differentiated with respect to y and evaluated at the wall such that

$$c_{p}\partial_{\nu}\widetilde{T}|_{w} = \|\boldsymbol{U}_{w}\|(\partial_{\nu}\|\widetilde{\boldsymbol{u}}\|)|_{w}\cos(\beta_{w}). \tag{A18}$$

By introducing  $\tau_w$  and  $q_w$ , the expression for  $\|U_w\|$  is then  $\|U_w\| = q_w Pr/\tau_w \cos(\beta_w)$ . Since  $\|U_w\|$  is defined with respect to wall quantities,  $\beta_w$  is chosen to be 0 such that  $U_w$  is parallel to  $\tau_w$  and  $e_{s,w}$ . Hence, combining the expression fro  $U_w$  and (A2) gives the modelled expression for  $\widetilde{T}$  from (5.1).

In Zhang *et al.* (2014), the expression for  $\phi$  gives  $T'' = Pr_t^{-1} \partial \widetilde{T} / \partial \widetilde{u}u''$  where  $Pr_t$  is a turbulent Prandtl number. This linear relationship between T'' and u'' is also reflected in the strong Reynolds analogy with stronger assumptions (Morkovin 1962). Motivated by these observations,  $\phi''$  is chosen such that a linear relationship emerges between T'' and  $u''_i$ . By taking the derivative of  $\widetilde{H}_g$  with respect to  $\|\widetilde{u}\|$ , it can be shown that

$$r_g = \frac{\|\boldsymbol{U}_w\|\cos(\beta)}{\|\widetilde{\boldsymbol{u}}\|} - \frac{c_p}{\|\widetilde{\boldsymbol{u}}\|} \frac{\partial \widetilde{T}}{\partial \|\widetilde{\boldsymbol{u}}\|}.$$
 (A19)

By using this expression in (A4), it can be shown that

$$c_p T'' - c_p \frac{\partial \widetilde{T}}{\partial \|\widetilde{\boldsymbol{u}}\|} \frac{\widetilde{u}_i}{\|\widetilde{\boldsymbol{u}}\|} u_i'' + c_p \phi'' = 0. \tag{A20}$$

In line with the results from the literature,  $\phi''$  is chosen to achieve a linear relationship between T'' and  $u''_i$  as

$$T'' = \left[ (1 - \cos(\beta)) \frac{Prq_w}{c_p \tau_w} + \frac{\partial \widetilde{T}}{\partial \|\widetilde{\boldsymbol{u}}\|} \right] e_{s,i} u_i''. \tag{A21}$$

By then multiplying (A21) with  $\rho v''$  and averaging, it can be shown that

$$\frac{\widetilde{v''T''}}{e_{s,i}\widetilde{v''u_i''}} - (1 - \cos(\beta))\frac{Prq_w}{c_p\tau_w} = \frac{\partial \widetilde{T}}{\partial \|\widetilde{\boldsymbol{u}}\|}.$$
 (A22)

It is important to note that because the second term on the left-hand side is small, (A22) suggests that  $\widetilde{v''T''}$  and  $e_{s,i}\widetilde{v''u''_i}$  are correlated. This is not entirely true, especially in the near-wall region of the  $\Pi=40$  cases. However, it is shown that this agreement holds in the outer region. Finally, by squaring both sides of (A20), multiplying by  $\rho$ , and averaging, provides the relationship in (5.3). Corrections for the lack of correlation between  $\widetilde{v''T''}$  and  $e_{s,i}\widetilde{v''u''_i}$  will in the future motivate better choices of  $\phi''$ .

### REFERENCES

And Anderson Jr., J.D. 2006 *Hypersonic and High-Temperature Gas Dynamics*, 2nd edn. American Institute of Aeronautics and Astronautics.

BAI, T., GRIFFIN, K.P. & FU, L. 2022 Compressible velocity transformations for various noncanonical wall-bounded turbulent flows. *AIAA J.* **60** (7), 4325–4337.

BENNEWITZ, J.W., BIGLER, B.R., HARGUS, W.A., DANCZYK, S.A. & SMITH, R.D. 2018 Characterization of detonation wave propagation in a rotating detonation rocket engine using direct high-speed imaging. In *Paper presented at 2018 Joint Propulsion Conference*, AIAA-2018-4688. AIAA.

BOAS, M.L. 2006 Mathematical Methods in the Physical Sciences. John Wiley & Sons.

BRADSHAW, P. 1977 Compressible turbulent shear layers. Annu. Rev. Fluid Mech. 9, 33-52.

BRADSHAW, P. & PONTIKOS, N.S. 1985 Measurements in the turbulent boundary layer on an 'infinite' swept wing. *J. Fluid Mech.* **159**, 105–130.

- BUSEMANN, A. 1931 Handbuch Der Experimentalphysik, vol. 4. Geest und Portig.
- CHANDRAN, D., ZAMPIRON, A., ROUHI, A., FU, M.K., WINE, D., HOLLOWAY, B., SMITS, A.J. & MARUSIC, I. 2023 Turbulent drag reduction by spanwise wall forcing. Part 2. High-Reynolds-number experiments. J. Fluid Mech. 968, A7.
- CHOI, J.-I., XU, C.-X. & SUNG, H.J. 2002 Drag reduction by spanwise wall oscillation in wall-bounded turbulent flows. AIAA J. 40 (5), 842–850.
- COGO, M., SALVADORE, F., PICANO, F. & BERNARDINI, M. 2022 Direct numerical simulation of supersonic and hypersonic turbulent boundary layers at moderate—high Reynolds numbers and isothermal wall condition. J. Fluid Mech. 945, A30.
- COLEMAN, G.N., KIM, J. & LE, A.-T. 1996 A numerical study of three-dimensional wall-bounded flows. *Intl J. Heat Fluid Flow* 17 (3), 333–342.
- COLEMAN, G.N., KIM, J. & MOSER, R.D. 1995 A numerical study of turbulent supersonic isothermal-wall channel flow. J. Fluid Mech. 305, 159–183.
- COLES, D. 1956 The law of the wake in the turbulent boundary layer. J. Fluid Mech. 1 (2), 191–226.
- CROCCO, L. 1932 Sulla trasmissione del calore da una lamina piana a un fluido scorrente ad alta velocita. L'Aerotecnica 12 (181–197), 126.
- DI RENZO, M., Fu, L. & URZAY, J. 2020 HTR solver: An open-source exascale-oriented task-based multi-GPU high-order code for hypersonic aerothermodynamics. *Comput. Phys. Commun.* **255**, 107262.
- DORODNITSYN, A. 1942 Laminar boundary layer in compressible fluid. Dokl. Akad. Nauk SSSR 34, 213-219.
- DUAN, L., BEEKMAN, I. & MARTIN, M.P. 2010 Direct numerical simulation of hypersonic turbulent boundary layers. Part 2. Effect of wall temperature. *J. Fluid Mech.* 655, 419–445.
- DUAN, L. & MARTIN, M.P. 2011 Direct numerical simulation of hypersonic turbulent boundary layers. Part 4. Effect of high enthalpy. J. Fluid Mech. 684, 25–59.
- FOWLER, M., ZAKI, T.A. & MENEVEAU, C. 2022 A Lagrangian relaxation towards equilibrium wall model for large eddy simulation. *J. Fluid Mech.* **934**, A44.
- GAVIGLIO, J. 1987 Reynolds analogies and experimental study of heat transfer in the supersonic boundary layer. Intl J. Heat Mass Transfer 30 (5), 911–926.
- GE, M. & JIN, G. 2017 Response of turbulent enstrophy to sudden implementation of spanwise wall oscillation in channel flow. Appl. Maths Mech. 38, 1159–1170.
- GOMEZ, S.R. 2025 Compressibility effects in a non-equilibrium three-dimensional supersonic turbulent boundary layer. In *CTR Annual Research Briefs*, pp. 65–78. CTR (Center for Turbulence Research).
- GRIFFIN, K.P., Fu, Lin & Moin, P. 2021 Velocity transformation for compressible wall-bounded turbulent flows with and without heat transfer. *Proc. Natl Acad. Sci.* 118 (34), e2111144118.
- GRIFFIN, K.P., Fu, L. & Moin, P. 2023 Near-wall model for compressible turbulent boundary layers based on an inverse velocity transformation. J. Fluid Mech. 970, A36.
- HARRISON, N.A., ANDERSON, J., FLEMING, J.L. & NG, W.F. 2013 Active flow control of a boundary layer-ingesting serpentine inlet diffuser. *J. Aircraft* **50** (1), 262–271.
- HASAN, A.M., COSTA, P., LARSSON, J., PIROZZOLI, S. & PECNIK, R. 2025 Intrinsic compressibility effects in near-wall turbulence. J. Fluid Mech. 1006, A14.
- HASAN, A.M., LARSSON, J., PIROZZOLI, S. & PECNIK, R. 2023 Incorporating intrinsic compressibility effects in velocity transformations for wall-bounded turbulent flows. *Phys. Rev. Fluids* 8 (11), L112601.
- HUANG, P.G., COLEMAN, G.N. & BRADSHAW, P. 1995 Compressible turbulent channel flows: DNS results and modelling. *J. Fluid Mech.* **305**, 185–218.
- KADER, B.A. 1981 Temperature and concentration profiles in fully turbulent boundary layers. *Intl J. Heat Mass Transfer* 24 (9), 1541–1544.
- KONG, H., CHOI, H. & LEE, J.S. 2000 Direct numerical simulation of turbulent thermal boundary layers. *Phys. Fluids* **12** (10), 2555–2568.
- LEE, M. & MOSER, R.D. 2015 Direct numerical simulation of turbulent channel flow up to  $Re_{\tau} \approx 5200$ . J. Fluid Mech. 774, 395–415.
- LEES, L. 1956 Laminar heat transfer over blunt-nosed bodies at hypersonic flight speeds. *J. Jet Propul.* **26** (4), 259–269.
- LELE, S.K. 1994 Compressibility effects on turbulence. Annu. Rev. Fluid Mech. 26 (1), 211-254.
- LOZANO-DURÁN, A., FLORES, O. & JIMÉNEZ, J. 2012 The three-dimensional structure of momentum transfer in turbulent channels. *J. Fluid Mech.* **694**, 100–130.
- LOZANO-DURÁN, A., GIOMETTO, M.G., PARK, G.I. & MOIN, P. 2020 Non-equilibrium three-dimensional boundary layers at moderate Reynolds numbers. *J. Fluid Mech.* 883, A20.
- MARUSIC, I., CHANDRAN, D., ROUHI, A., FU, M.K., WINE, D., HOLLOWAY, B., CHUNG, D. & SMITS, A.J. 2021 An energy-efficient pathway to turbulent drag reduction. *Nat. Commun.* 12 (1), 5805.
- MILLIKAN, C.B. 1938 A critical discussion of turbulent flows in channels and circular tubes. In *Proceedings* of the Fifth International Congress for Applied Mechanics. p. 386–392. Wiley.

## S.R. Gomez

- MODESTI, D. & PIROZZOLI, S. 2016 Reynolds and mach number effects in compressible turbulent channel flow. *Intl J. Heat Fluid Flow* **59**, 33–49.
- MOIN, P., SHIH, T.-H., DRIVER, D. & MANSOUR, N.N. 1990 Direct numerical simulation of a three-dimensional turbulent boundary layer. *Phys. Fluids A: Fluid Dyn.* 2 (10), 1846–1853.
- MORKOVIN, M.V. 1962 Effects of compressibility on turbulent flows. Méc. Turbul. 367 (380), 26.
- NAGANO, Y. & TAGAWA, M. 1988 Statistical characteristics of wall turbulence with a passive scalar. J. Fluid Mech. 196, 157–185.
- NI, W., Lu, L., RIBAULT, C.L. & FANG, J. 2016 Direct numerical simulation of supersonic turbulent boundary layer with spanwise wall oscillation. *Energies* **9** (3), 154.
- PERRY, A.E. & HOFFMANN, P.H. 1976 An experimental study of turbulent convective heat transfer from a flat plate. *J. Fluid Mech.* 77 (2), 355–368.
- PERRY, A.E. & MARUSIC, I. 1995 A wall-wake model for the turbulence structure of boundary layers. Part 1. Extension of the attached eddy hypothesis. J. Fluid Mech. 298, 361–388.
- PIROZZOLI, S. 2012 On the size of the energy-containing eddies in the outer turbulent wall layer. *J. Fluid Mech.* **702**, 521–532.
- PIROZZOLI, S. & BERNARDINI, M. 2011 Turbulence in supersonic boundary layers at moderate Reynolds number. J. Fluid Mech. 688, 120–168.
- PIROZZOLI, S., BERNARDINI, M. & ORLANDI, P. 2016 Passive scalars in turbulent channel flow at high Reynolds number. *J. Fluid Mech.* **788**, 614–639.
- QUADRIO, M. & SIBILLA, S. 2000 Numerical simulation of turbulent flow in a pipe oscillating around its axis. *J. Fluid Mech.* **424**, 217–241.
- REYNOLDS, O. 1874 On the extent and action of the heating surface of steam boilers. Proc. Lit. Phil. Soc. Manchester 14, 7–12.
- RICCO, P., SKOTE, M. & LESCHZINER, M.A. 2021 A review of turbulent skin-friction drag reduction by near-wall transverse forcing. *Prog. Aerosp. Sci.* 123, 100713.
- ROUHI, A., FU, M.K., CHANDRAN, D., ZAMPIRON, A., SMITS, A.J. & MARUSIC, I. 2023 Turbulent drag reduction by spanwise wall forcing. Part 1. Large-eddy simulations. *J. Fluid Mech.* **968**, A6.
- SCHLICHTING, H. & GERSTEN, K. 2016 Boundary-Layer Theory. Springer.
- SUBBAREDDY, P.K., BARTKOWICZ, M.D. & CANDLER, G.V. 2014 Direct numerical simulation of high-speed transition due to an isolated roughness element. *J. Fluid Mech.* **748**, 848–878.
- TOWNSEND, A.A.R. 1976 The Structure of Turbulent Shear Flow. Cambridge University Press.
- TRETTEL, A. & LARSSON, J. 2016 Mean velocity scaling for compressible wall turbulence with heat transfer. Phys. Fluids 28 (2), 026102.
- VAN DRIEST, E. 1951 Turbulent boundary layer in compressible fluids. J. Aeronaut. Sci. 18 (3), 145-160.
- VON KÁRMÁN, T. 1934 Turbulence and skin friction. J. Aeronaut. Sci. 1 (1), 1–20.
- Vos, R. & FAROKHI, S. 2015 Introduction to Transonic Aerodynamics, vol. 110. Springer.
- WALLACE, J.M. 2016 Quadrant analysis in turbulence research: history and evolution. Annu. Rev. Fluid Mech. 48 (1), 131–158.
- WALLACE, J.M., ECKELMANN, H. & BRODKEY, R.S. 1972 The wall region in turbulent shear flow. *J. Fluid Mech.* **54** (1), 39–48.
- WALZ, A. 1962 Compressible Turbulent Boundary Layers. CNRS.
- YAO, J. & HUSSAIN, F. 2019 Supersonic turbulent boundary layer drag control using spanwise wall oscillation. J. Fluid Mech. 880, 388–429.
- YU, M., XU, C.-X. & PIROZZOLI, S. 2019 Genuine compressibility effects in wall-bounded turbulence. *Phys. Rev. Fluids* 4 (12), 123402.
- ZHANG, Y.-S., BI, W.-T., HUSSAIN, F., LI, X.-L. & SHE, Z.-S. 2012 Mach-number-invariant mean-velocity profile of compressible turbulent boundary layers. *Phys. Rev. Lett.* **109** (5), 054502.
- ZHANG, Y.-S., BI, W.-T., HUSSAIN, F. & SHE, Z.-S. 2014 A generalized Reynolds analogy for compressible wall-bounded turbulent flows. *J. Fluid Mech.* **739**, 392–420.